



# Investigating synergistic effects of process-induced defects and $\alpha$ phase substructures on the mechanical response of additively manufactured Ti-6Al-4V alloy via an integrated numerical framework

Hanqing Liu<sup>a, \*</sup>, Fabien Briffod<sup>b</sup>, Takayuki Shiraiwa<sup>a, \*</sup>

<sup>a</sup> Department of Materials Engineering, The University of Tokyo, 7-3-1 Hongo, Bunkyo-ku, Tokyo, 113-8656, Japan

<sup>b</sup> Research Center for Structural Materials, National Institute of Materials Science, 1-2-1 Sengen, Tsukuba, Ibaraki, 305-0047, Japan

## ARTICLE INFO

### Keywords:

Ti-6Al-4V

Additive manufacturing

Defect

$\alpha$ -phase substructure

Cellular automaton

Crystal plasticity finite element method

Tensile

## ABSTRACT

Laser powder bed fusion (LPBF)-fabricated Ti-6Al-4V alloys are characterized by complex  $\alpha$ -lath substructures and inherent process-induced defects. While numerical investigations are prevalent, conventional models often oversimplify microstructural morphologies and defects, leading to deviations in predicting failure mechanisms. In this study, a novel approach integrating cellular automaton (CA) with an algorithm-based structure generation method is proposed to address these limitations. In this framework, the CA technique is first employed to simulate the growth of prior- $\beta$  columnar grains. Subsequently, an ellipse-fitting method is developed to construct the  $\alpha$ -lath substructure, where the  $\beta$ -to- $\alpha$  phase transformation is achieved based on the Burgers orientation relationship (BOR). The Monte Carlo (MC) method is utilized to construct an irregular defect based on experimental characteristics. Through a comparative study between observations and crystal plasticity finite element method (CPFEM) simulations, the synergistic roles of the  $\alpha$ -lath substructure and defects on the resulting tensile responses are evaluated. It is found that basal and pyramidal ( $\alpha$ ) slip systems might be responsible for the crack initiation from the defect tips. Neglecting  $\alpha$ -lath substructure results in a stress distribution overly dependent on prior- $\beta$  grain boundaries and a marked underestimation of local stress/strain concentrations. The presence of defects is harmful to structural integrity and facilitate strain localization between defects, thereby accelerating the onset of localized failure and resulting in a zigzag-shaped fracture surface. The proposed microstructure construction strategy addresses the inherent shortcomings of traditional modeling methods and provides a robust tool for evaluating the mechanical behavior of additively manufactured metallic alloys.

## 1. Introduction

Metal components in the aerospace, automobiles, and space technology fields are increasingly driven by the demand for superior strength-to-weight ratios and highly complex geometries, which are often unattainable through traditional subtractive manufacturing methods [1,2]. In recent years, these challenges have been effectively addressed by additive manufacturing (AM) technology. This technology facilitates the fabrication of topology-optimized hollow lattice structures and offers a high degree of design freedom [3]. Laser powder bed fusion (LPBF) is an AM technique that utilizes a high-energy laser beam to selectively melt metallic powder layer-by-layer [4]. Following a computer-aided scanning strategy, the laser scans pre-defined cross-sections on a build platform, enabling the building of complex

three-dimensional geometries. Ti-6Al-4V alloy exhibits superb corrosion resistance and high strength [5,6], accounting for nearly a half of the market share of titanium products [7]. However, Ti-6Al-4V is conventionally classified as a difficult-to-machine material due to its low thermal conductivity, high chemical reactivity, and low elastic modulus, which often results in excessive waste materials and rapid tool consumption during traditional subtractive manufacturing [8]. Since these challenges can be effectively mitigated by AM technologies, the fabrication of Ti-6Al-4V components via LPBF has emerged as a popular research focus in recent years.

LPBF technology delivers high dimensional accuracy while enables the fabricated Ti-6Al-4V components with desirable tensile strength and ductility. Numerous studies have confirmed the exceptional mechanical performance of LPBF-fabricated Ti-6Al-4V components. For instance, Z.

\* Corresponding author.

E-mail address: [shiraiwa@rme.mm.t.u-tokyo.ac.jp](mailto:shiraiwa@rme.mm.t.u-tokyo.ac.jp) (T. Shiraiwa).

<https://doi.org/10.1016/j.msea.2026.150551>

Received 24 March 2026; Received in revised form 21 May 2026; Accepted 1 June 2026

Available online 5 June 2026

0921-5093/© 2026 The Authors. Published by Elsevier B.V. This is an open access article under the CC BY license (<http://creativecommons.org/licenses/by/4.0/>).

Xu et al. [9] demonstrated that the fatigue limit and crack propagation resistance of a LPBF prostheses can rival those of conventional rolled products in fatigue condition, specifically for products built in  $0^\circ$  and  $45^\circ$  direction. Furthermore, the inherently formed  $\alpha'$  martensite phase during the rapid cooling of LPBF has been reported to significantly enhance the ultimate tensile and yield strength by 100–200 MPa [7,10,11]. While LPBF offers significant benefits, it inherently brings about detrimental impacts on the fabricated components, especially the process-induced defects.

Due to the high cooling rates, LPBF-fabricated Ti-6Al-4V is highly susceptible to porosity compared to conventionally processed counterparts [11]. Generally, two distinct types of defects are observed in LPBF products: gas pores and lack-of-fusion (LOF) voids [12]. Gas pores originate from gas entrapment during the rapid solidification process and typically exhibit a spherical morphology. In contrast, LOF voids show a more complex, irregular morphology, which serves as a primary driver for the observed scatter in mechanical performance [13]. Through the characterization of fracture surfaces, A. Gupta et al. [12] suggested that defects are responsible for the detrimental impact on the ductility of as-built Ti-6Al-4V. Likewise, L. Bhandari and V. Gaur [14] identified that defects are frequently situated near fatigue crack initiation sites, concluding that surface and sub-surface defects act as the primary crack precursors and are significantly more harmful. J. Elambasseril et al. [13] statistically analyzed the spatial distribution of defects in Ti-6Al-4V components produced via deep-powder-bed manufacturing and evaluated their subsequent impact on tensile properties. Although it is well-established that LPBF-induced defects accelerate crack initiation and propagation, current understanding remains largely qualitative and inferential [15]. A more transparent and direct quantification of the specific role that defects play in localized failure remains a significant challenge.

In addition to process-induced defects, the variation in energy input rate and laser scanning strategy during LPBF also gives rise to a diverse range of non-homogeneous microstructural morphologies in Ti-6Al-4V, which exerts a profound influence on the mechanical performance of the fabricated components [16–18]. Typically, LPBF-processed Ti-6Al-4V exhibits lamellar prior- $\beta$  grains aligned with the deposition direction. Within these prior- $\beta$  grains, needle-like martensitic  $\alpha'$  phase forms as a result of a rapid cooling rate [19]. While the presence of the martensitic  $\alpha'$  phase yields significantly higher strength compared to wrought counterparts, it is typically accompanied by a concomitant reduction in ductility [20]. G. Lütjering [21] suggested that the colony size acts as a critical structural parameter that limits the dislocation slip length, and thereby influence the yield strength and ductility. J. Liu et al. [15] observed that the coarse  $\alpha$ -laths adjacent to defects are more favorable for deformation and stronger micro-texture for slip transmission.

While these findings offer valuable insights into the role of defects and  $\alpha$ -laths in determining mechanical properties, the inherent complexity and heterogeneity of LPBF-processed microstructures make comprehensive experimental investigations time-consuming and resource-intensive. Crystal plasticity finite element method (CPFEM) simulation has become as a widely adopted methodology for studying LPBF-processed Ti-6Al-4V, primarily due to its cost-effectiveness and capacity for quantitative analysis [22–24]. The Voronoi tessellation (VT) method is the most widely applied modeling strategy, due to its computational efficiency and statistical representativeness of equiaxed morphologies [25]. By partitioning a spatial domain into cells based on a set of randomly distributed seed points, the VT method constructs synthetic polycrystalline geometries. However, this approach is incapable of capturing the characteristic microstructural heterogeneities inherent to LPBF-fabricated Ti-6Al-4V. Cellular automaton (CA) technique generates microstructures by simulating the physical phenomena of laser melting, grain nucleation, and solidification [26]. This approach allows a more realistic representation of microstructural features, capturing the non-equilibrium growth inherent to the LPBF process.

While CA techniques are widely employed for predicting the microstructures of LPBF-fabricated alloys [27–29], their application is often restricted to generating defect-free and single-phase grains. As a representative  $\alpha + \beta$  dual-phase titanium alloy, Ti-6Al-4V has complex lath-shaped  $\alpha$  phase microstructure inside of prior- $\beta$  grain, which makes it a significant challenge for high-fidelity reconstruction using CA methods alone. Nevertheless, existing numerical frameworks frequently overlook the synergistic impact of defects and  $\alpha$ -lath substructures [24]. These critical features are often simplified or omitted in conventional models, leading to a potential gap in predicting the localized mechanical response of LPBF-fabricated Ti-6Al-4V alloy [22,30–32].

Although numerous studies have highlighted the critical roles of process-induced defects and  $\alpha$ -lath substructures in the failure mechanisms of LPBF-fabricated Ti-6Al-4V, these features remain insufficiently represented in most numerical investigations. To address these limitations, the present study developed a multi-scale numerical framework coupling CA and CPFEM to investigate the synergistic effects of process-induced defects and  $\alpha$  substructures on the mechanical response of LPBF-fabricated Ti-6Al-4V alloy. In this framework, the CA technique is first employed to simulate the epitaxial growth of prior- $\beta$  columnar grains. Subsequently, a statistical ellipse-fitting method is proposed to construct the  $\alpha$ -lath substructure, where the  $\beta$ -to- $\alpha$  phase transformation is conducted by the minimum elastic strain energy indicator rule [16] based on the Burgers orientation relationship (BOR). The MC method is utilized to reconstruct an irregular defect based on experimental statistical characteristics. Finally, the localized stress-strain evolution and the overall tensile response of LPBF-processed Ti-6Al-4V alloy are investigated with a crystal plasticity constitutive model by CPFEM. This study develops a statistics-based microstructure construction strategy for numerical modeling, which enhances the capability to predict mechanical properties and investigate failure mechanisms in LPBF-fabricated alloys.

## 2. Experimental methods

### 2.1. Material

The Ti-6Al-4V alloy specimens in this study were fabricated with an Aconity MINI (Aconity 3D) system under an argon atmosphere, utilizing commercial powder from Osaka Titanium Technologies Co., Ltd. The processing parameters included a laser power of 250 W, a scanning speed of 400 mm/s, a hatch spacing of 80  $\mu\text{m}$ , a layer thickness of 30  $\mu\text{m}$ , and a focal spot diameter of 80  $\mu\text{m}$ . Rectangular blocks with dimensions of 10 mm  $\times$  10 mm  $\times$  80 mm were vertically fabricated using an X-Y scanning strategy, followed by machining into standard tensile specimens as illustrated in Fig. 1 (a). A 10 mm  $\times$  10 mm  $\times$  5 mm block was cut from the bulk specimen for observation. The specimen surfaces were prepared by manual mechanical grinding using a progressive series of SiC abrasive papers from 180 to 4500 grit. This was followed by 3  $\mu\text{m}$   $\text{Al}_2\text{O}_3$ -based suspension and final polishing with colloidal silica (OPS). After mechanical polishing, the specimens were treated with ion beam milling using a UT-158 cross-section polisher to ensure a high-quality surface finish. Scanning electron microscopy (SEM) and electron backscatter diffraction (EBSD) observations were conducted with a JSM-7000F field-emission scanning electron microscope. SEM morphologies were acquired in secondary electron imaging (SEI) mode at an accelerating voltage of 10.0 kV with a working distance of 10.0 mm. EBSD data were acquired at an accelerating voltage of 20.0 kV and a working distance of 20.0 mm. A step size of 0.5  $\mu\text{m}$  was employed for broad-area orientation mapping, while a finer step size of 0.1  $\mu\text{m}$  was utilized for high-resolution characterization of localized regions. Numerous defects are visible in the SEM image of the specimen surface as shown in Fig. 1 (b), where the building direction (BD) is oriented horizontally as indicated. The inverse pole figure (IPF) map and pole figures (PF) of the  $\alpha$  phase, obtained from EBSD results, are shown in Fig. 1 (c) and 1 (d), respectively. EBSD mapping reveals fine lath-shaped  $\alpha$  grains. Phase analysis indicates that the  $\alpha$  phase volume fraction is as

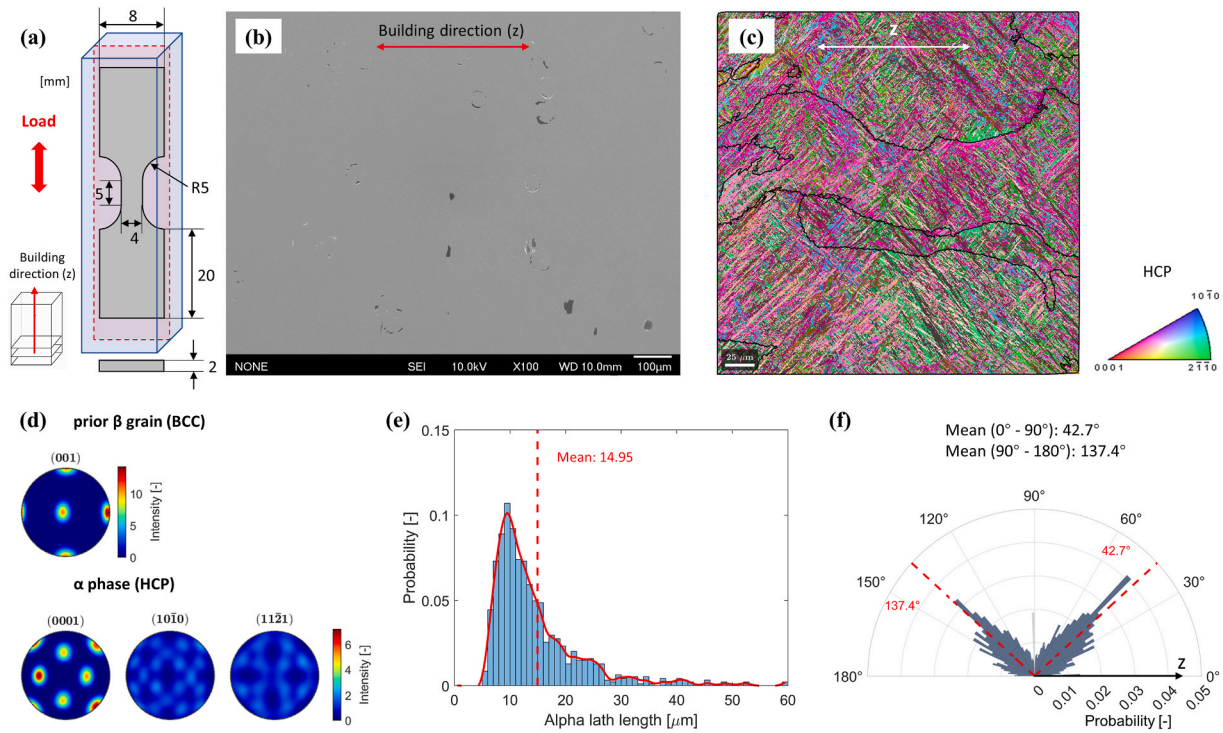


**Fig. 1.** Characterization of LPBF-fabricated Ti-6Al-4V specimen. (a) Building direction, load direction and specimen dimensions. (b) SEM image of specimen surface. (c) Inverse pole figure map of  $\alpha$  phase with recalculated prior- $\beta$  grain boundaries. (d) Pole figures of recalculated prior- $\beta$  grain and  $\alpha$  phase. (e) Probability density distribution of  $\alpha$ -lath length. (f) Probability density distribution of the inclination angle between the major axis of the  $\alpha$ -lath and the LPBF building direction.

high as 99.9%. The prior- $\beta$  grains, reconstructed using the open-source MATLAB toolbox MTEX, exhibit a lamellar-like microstructure along the BD. Despite the laser parameters involved in this work differing from our previous studies, the PFs display a similar peak distribution [16]. To further characterize the morphological features of  $\alpha$  grains, the distributions of lath length and orientation to the BD are presented in Fig. 1 (e) and 1 (f), respectively. Due to the step size limitations during the EBSD scanning process, the raw orientation map contained numerous isolated single-pixel points. To accurately characterize the morphological features of the  $\alpha$ -laths, a grain reconstruction procedure was performed using the open-source MATLAB toolbox, MTEX. During this process, a denoising filter was applied, where grains consisting of only a single pixel were excluded to ensure the statistical reliability of the identified lath boundaries. The  $\alpha$ -laths exhibit an average length of 14.95  $\mu\text{m}$ , with a broad distribution spanning approximately 5.0  $\mu\text{m}$  to 60.0  $\mu\text{m}$ . Two distinct preferred orientations of  $\alpha$ -laths are observed. To more clearly describe these orientation characteristics, the lath orientations were categorized into two groups:  $0^\circ$ – $90^\circ$  and  $90^\circ$ – $180^\circ$ . The mean values for these groups were determined to be  $42.7^\circ$  and  $137.4^\circ$ , respectively.

## 2.2. Tensile test conditions

Tensile tests were performed at room temperature using a Shimadzu EHF-E testing machine with maximum load capacity of 50 kN under strain-controlled conditions with a strain rate of  $0.001 \text{ s}^{-1}$ . The dog bone-shaped specimen was fixed by hydraulic clamps. An Epsilon 3442-GL8-0.5 mm extensometer was attached to the middle part of the specimen by two clips. The extensometer measurements were recorded up to approximately 5% strain, after which the test was continued until the specimen completely fractured. The fracture surfaces were characterized using a JEOL JCM-6000 SEM.

## 3. Numerical methods

The workflow of the integrated numerical framework developed in this study is illustrated in Fig. 2. Initially, the LPBF process parameters and the corresponding material properties of Ti-6Al-4V were incorporated into CA simulation process to construct a representative lamellar prior- $\beta$  grain microstructure. Subsequently, the  $\alpha$ -lath substructure was reconstructed using an ellipse-fitting algorithm based on EBSD data. The  $\beta$ -to- $\alpha$  phase transformation was conducted with a minimum elastic strain energy indicator rule.

To incorporate manufacturing uncertainties, polygonal defects were stochastically generated via the MC method, utilizing morphological data extracted from SEM observations. The fidelity of the defect generation was further validated against nine critical geometric parameters. Finally, a crystal plasticity (CP) model was obtained by integrating the reconstructed  $\alpha$ -lath substructure and defect. After calibrating the CP parameters against experimental tensile data, CPFEM simulations were performed across various models to systematically investigate the synergistic effects of process-induced defects and  $\alpha$ -lath substructure on the localized mechanical response.

### 3.1. Cellular automaton procedure

The CA simulation was carried out with the commercial FEM solver Abaqus and an open-source software ExaCA [26]. A Gaussian-distributed thermal field of single laser trace was first obtained through a user-defined material subroutine (UMAT) in Abaqus. The model utilized a mesh of  $200 \times 200 \times 100$  with a mesh size of 1  $\mu\text{m}$  and employed 8-node hexahedral elements (C3D8R). The bottom surface of model was fixed at a constant temperature of 298 K. The laser scanning process was modeled by applying a time-dependent surface heat flux to represent the moving laser. Detailed material properties used for the simulation are shown in Table 1. Subsequently, this single-laser-track thermal field was utilized to generate the full LPBF temperature history under a X-Y scanning strategy by translational and rotational

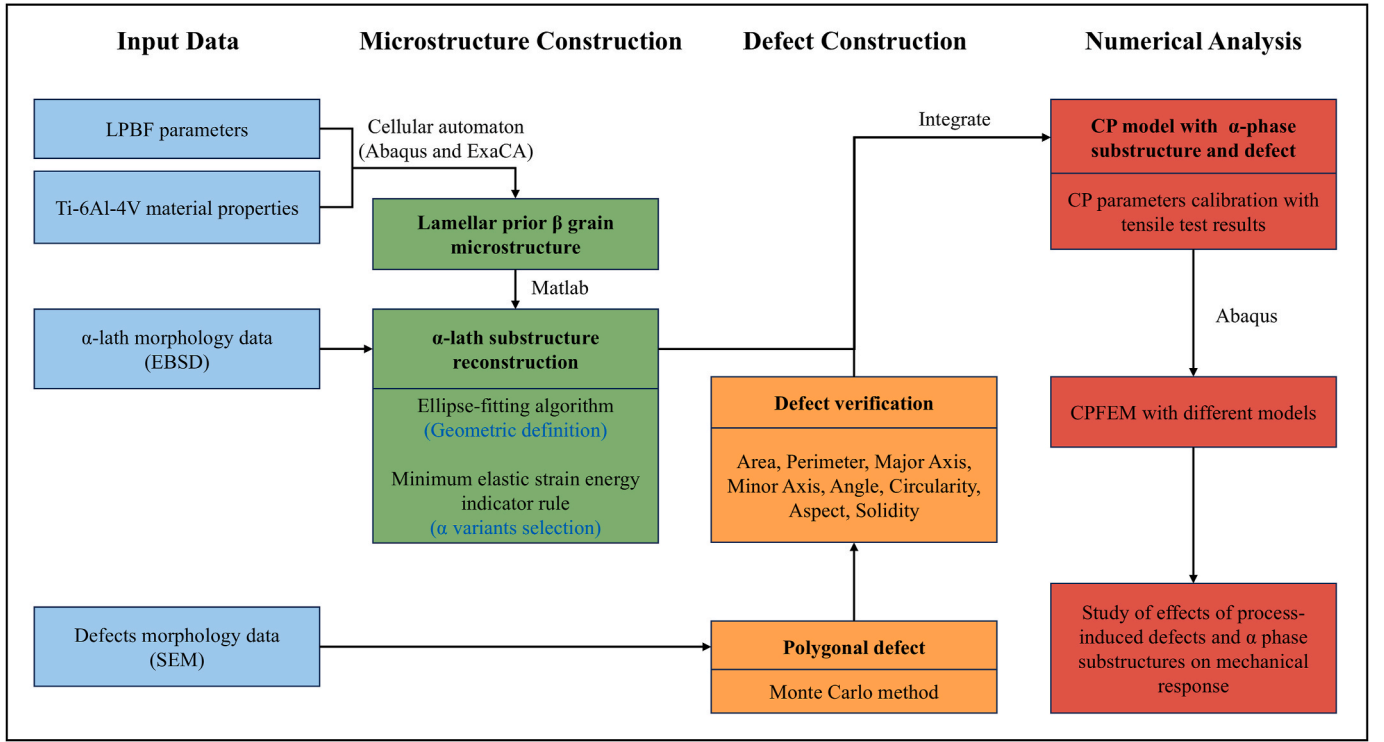


Fig. 2. The workflow of the integrated numerical framework.

Table 1

Material constants for Ti-6Al-4V in CA process.

conductivity [W/(m·K)]	density [kg/m <sup>3</sup> ]	specific Heat [J/(kg·K)]
7.5	4430	520

coordinate transformations. Finally, a rectangular block model was constructed by stacking 32 layers along the BD, which was designated as the z-axis in the simulation coordinate system. Crystal nucleation and grain growth were simulated using ExaCA based on the previously obtained rectangular block thermal history. During the simulation, the laser parameters were aligned with actual values employed in the LPBF process. The nucleation density was set to  $3 \times 10^4 \text{ mm}^{-3}$ . A  $200 \times 200$  pixels cross-sectional region was extracted from the vertical plane of the final CA model for further microstructural analysis.

### 3.2. The $\alpha$ -lath substructure construction procedure

Given that the  $\alpha$  grains exhibit a narrow lath-like morphology, an ellipse-fitting method was employed to reconstruct the  $\alpha$ -lath substructure within the CA-generated model, as illustrated in Fig. 3 (a). Ellipses with varying major axis lengths and orientations were generated within the prior- $\beta$  grains. Then, the encapsulated elements were designated as members of specific  $\alpha$ -laths. During this procedure, the  $\alpha$ -lath major axis length probability distribution was adapted as the function to match the experimental distribution trend. The  $200 \times 200$  pixels domain was extended to  $400 \times 400$  pixels, effectively reducing the mesh size to  $0.5 \mu\text{m}$  to ensure geometric continuity of  $\alpha$ -laths. Any remaining isolated single-pixel elements were subsequently removed from the model to eliminate numerical artifacts.

### 3.3. Phase transformation method

As a typical dual-phase alloy, the  $\alpha$  phase and prior- $\beta$  phase in Ti-6Al-4V satisfy the BOR, which is defined as  $\{110\}_{\beta} // (0001)_{\alpha}$  and  $\langle 1\bar{1}1 \rangle_{\beta} /$

$\langle 11\bar{2}0 \rangle_{\alpha}$  [33]. However, the BOR allows for up to 12 distinct  $\alpha$ -variants from a single  $\beta$ -orientation, making it computationally prohibitive to include all possibilities in a digital model. To address this, a minimum elastic strain energy indicator rule was proposed in our previous work and has been proven effective for variant selection [16].

In this study, rather than selecting a single dominant variant, six  $\alpha$ -variants with the lowest elastic strain energy indicators  $E_{\text{elastic}}^i$  were identified as candidates for each  $\alpha$ -lath. The selection is governed by:

$$\text{Variant index} \in \arg \text{sort}_k \{ E_{\text{elastic}}^i \}, k = 1, \dots, 6 \quad (1)$$

where  $i$  denotes the index of the 12 possible  $\alpha$  variants according to BOR, and  $E_{\text{elastic}}^i$  is the corresponding elastic strain energy indicator.

After selecting the six  $\alpha$ -variants, the crystal orientations corresponding to each variant were assigned to the respective elements within the  $\alpha$ -lath structure, which had been reconstructed using the ellipse-fitting method.

### 3.4. Monte Carlo method-based defect generating procedure

To quantitatively characterize the morphological features of LPBF-induced defects, several key parameters, including area ( $A$ ), perimeter ( $P$ ), major axis length ( $a$ ), and minor axis length ( $b$ ), were extracted from SEM images of 47 LOF defects. Based on these fundamental metrics, the circularity ( $C$ ) is calculated to evaluate how closely the defect shape approximates a perfect circle, while aspect ratio ( $AR$ ) and roundness ( $R$ ) are used to represent the geometric elongation of the defect. Solidity ( $S$ ) is determined to measure the morphological density and boundary irregularity of the defect structure.

A polygonal defect was constructed using the MC method, as illustrated in Fig. 3 (b). Initially, a set of random vertex coordinates was generated to form a seed polygon within the prescribed domain. The algorithm then iteratively perturbed these coordinates by applying small, random displacements. After each step, the morphological features of the evolving polygon were recalculated and compared against the target experimental mean values to ensure geometric fidelity. Once



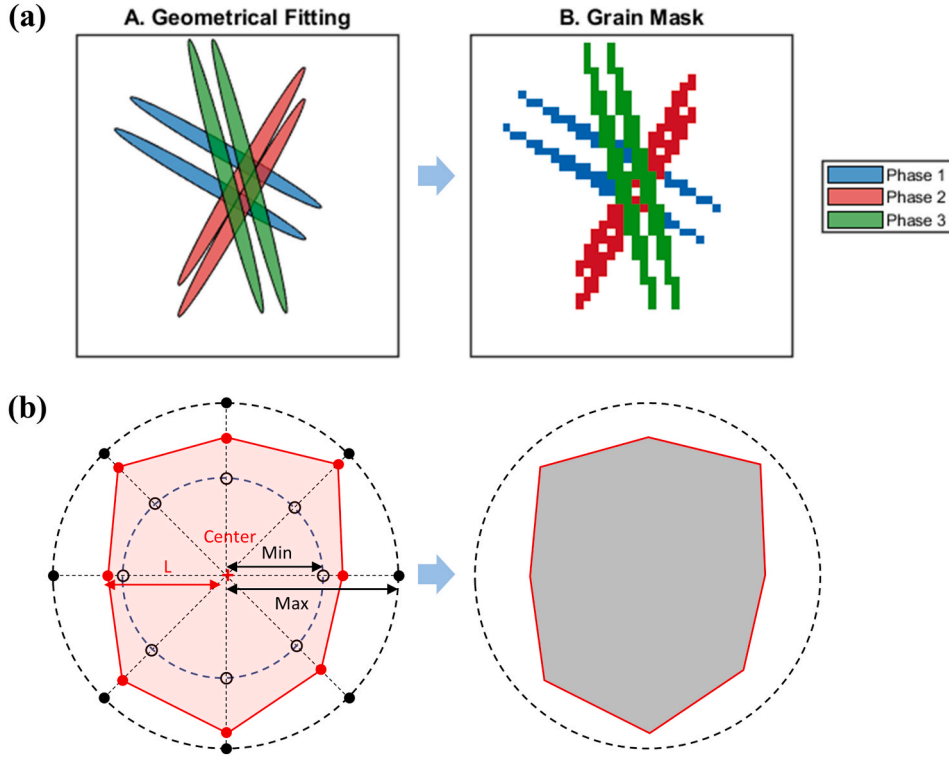


**Fig. 3.** Schematic illustration of (a) the  $\alpha$  phase substructure construction based on the ellipse-fitting method and (b) the polygonal defect generation process based on the Monte Carlo method.

the polygonal geometry reached an acceptable deviation from the target experimental mean values, it was integrated into the numerical model as a pre-existing defect.

### 3.5. Crystal plasticity constitutive model

To perform the CPFEM simulation, a rate-dependent crystal plasticity constitutive model is applied in this study achieved by UMAT in Abaqus [16,34]. In this numerical framework, the mechanical response is governed by the total deformation gradient  $\mathbf{F}$ , which can be partitioned into elastic gradient  $\mathbf{F}^e$  for lattice stretch and rigid body rotation and plastic gradient  $\mathbf{F}^p$  for dislocation slip. Since twinning is significantly suppressed in the Ti-6Al-4V alloy due to its high aluminum content and is rarely observed in this specific alloy system [32,35]. Consequently, twinning mechanisms are not incorporated into the present crystal plasticity constitutive model.

The kinematic evolution of the plastic state is tracked via the plastic velocity gradient  $\mathbf{L}^p$ , which is defined by the crystallographic shearing rates  $\dot{\gamma}^i$  summed over the active slip systems:

$$\mathbf{L}^p = \dot{\mathbf{F}}^p (\mathbf{F}^p)^{-1} = \sum_{i=1}^N \dot{\gamma}_0 \left| \frac{\tau^i}{g^i} \right|^{\frac{1}{m}} \text{sgn}(\tau^i) (\mathbf{s}^i \otimes \mathbf{n}^i) \quad (2)$$

where  $\mathbf{s}^i$  and  $\mathbf{n}^i$  are vectors in slip plane direction and the slip plane normal for the  $i^{\text{th}}$  slip system, respectively.  $\dot{\gamma}_0$  represents the reference slip rate. To enhance computational efficiency while maintaining physical consistency,  $\dot{\gamma}_0$  is assumed to be uniform across all slip systems.  $g^i$  represents the slip resistance for the  $i^{\text{th}}$  slip system, acting as the threshold for slip activation. The  $\frac{1}{m}$  represents the strain rate sensitivity.

The current slip resistance  $g^i$  is based on a multi-term strengthening law:

$$g^i = \tau_0^i + \tau_{HP}^i + \tau_{slip}^i \quad (3)$$

where  $\tau_0^i$  is the initial critical resolved shear stress (CRSS) for the  $i^{\text{th}}$  slip system, and  $\tau_{slip}^i$  is the hardening rate due to slip-slip interactions. The term  $\tau_{HP}^i$  represents microstructure-dependent Hall-Petch strengthening [36,37], which scales with the effective slip length  $d_{eff}^i$ :

$$\tau_{HP}^i = \frac{k_{HP}}{\sqrt{d_{eff}^i}} \quad (4)$$

where  $k_{HP}$  is the Hall-Petch contribution coefficient, and  $d_{eff}^i$  is determined by the microstructural dimension of the free slip length, which corresponds to the  $\alpha$ -lath thickness in the present study. Due to the constraints of the model resolution, a uniform  $\alpha$ -lath thickness is adapted throughout the model, rendering the Hall-Petch contribution constant across all  $\alpha$ -laths. To streamline the model calibration and reduce parametric redundancy, the term  $\tau_{HP}^i$  in the models with  $\alpha$ -lath substructure is subsumed into terms  $\tau_0^i$ . In contrast, for models without  $\alpha$ -lath substructure,  $\tau_{HP}$  is calculated based on prior- $\beta$  grain size, reflecting the effect of increasing mean free path for dislocation motion [16,34,38].

The slip-slip hardening rate  $\tau_{slip}^i$  is expressed as a function of the cumulative shear strain  $\Gamma$  and the latent hardening interactions among all active slip systems  $\tau_{S \rightarrow S}^{(i)}$ :

$$\tau_{slip}^i = \int_t \dot{\tau}_{slip}^i dt \quad (5)$$

$$\dot{\tau}_{slip}^i = \frac{\tau_{S \rightarrow S}^i}{d\Gamma} \sum_j^n h_{ij} |\dot{\gamma}^j| \quad (6)$$

$$\Gamma = \sum_i^n \int_t |\dot{\gamma}^{(i)}| dt \quad (7)$$

where  $n$  is the total slip system number, and  $h_{ij}$  is the hardening coef-

ficient representing the interaction among  $i^{\text{th}}$  and  $j^{\text{th}}$  slip systems.

The term  $\tau_{s \rightarrow s}^i$  is modeled via an extended Voce-type saturation criterion:

$$\tau_{s \rightarrow s}^i = \left( \tau_1^i + h_1^i \Gamma \right) \left( 1 - \exp \left( - \frac{b_1^i}{\tau_1^i} \Gamma \right) \right) \quad (8)$$

where  $\tau_1^i$ ,  $h_1^i$  and  $b_1^i$  is saturated CRSS, initial hardening rate and asymptotic hardening rate for  $i^{\text{th}}$  slip systems, respectively. In this study, these parameters were assumed to be the same for all slip systems [16, 39].

### 3.6. Numerical simulations

To systematically investigate the influence of defects and  $\alpha$  phase microstructural features, four distinct simulation cases were established: a model with defects and  $\alpha$ -lath substructure (DS), a model without defects but with  $\alpha$ -lath substructure (NDS), a model with defects but without  $\alpha$ -lath substructure (DNS), and a model without defects and  $\alpha$ -lath substructure (NDNS). Each model has a dimension of  $200 \mu\text{m} \times 200 \mu\text{m} \times 0.5 \mu\text{m}$  with a voxel size of  $0.125 \mu\text{m}^3$ . The crystallographic orientation properties of these models were assigned based on the phase transformation results as discussed in Section 3.3. The boundary conditions remain consistent across all simulations. Symmetric constraints are applied by fixing the left, bottom, and front surfaces in their respective normal directions. Uniaxial loading was implemented by prescribing a constant strain rate of  $0.001 \text{ s}^{-1}$  at the top surface along the y-axis.

## 4. Results

### 4.1. Specimen surface observations

The surface morphologies before tensile testing are presented in Fig. 4. High-magnification SEM images reveal the distinct characteristics of a LOF defect and a gas pore in Fig. 4 (a) and 4 (b), respectively. The LOF defect is characterized by a large, irregularly shaped void containing several unmelted Ti-6Al-4V powder particles. In contrast, the gas pore exhibits a characteristic spherical morphology with a smooth internal boundary. Generally, optimizing the laser energy input is an effective strategy for mitigating LPBF-induced defects [40]. However, an excessively high energy density can lead to a higher porosity, typically associated with the transition into the keyhole melting regime [13,41]. This explains why defects were absent from our previous work but are prevalent in the current study, despite the energy density employed here

being significantly higher. To further investigate the localized influence of defects on the  $\alpha$  phase microstructure, an EBSD scan was performed over a  $300 \mu\text{m} \times 300 \mu\text{m}$  region, as shown in Fig. 4 (c). The defects are readily identifiable as non-indexed black regions, within which only sparse colored pixels are observed. Correlation with the SEM image reveals that these regions were occupied by large particles. The absence of clear orientation mapping for these particles is attributed to the sample preparation process. During mechanical polishing and ion beam milling processes, the particles suspended within the voids lacked rigid support. Consequently, their surface topography became unsuitable for high-quality Kikuchi pattern recognition, leading to low indexing rates in the EBSD results. A high-magnification EBSD map, focusing on the region highlighted by the red circle in Fig. 4 (c), was acquired using a refined step size and is presented in Fig. 4 (d). No significant microstructural anomalies or preferential grain orientations were observed near the defect boundaries. This observation suggests that the presence of LPBF-induced defects does not perceptibly interfere with the nucleation and subsequent growth kinetics of the  $\alpha$  phase. This observation reveals that microstructure formation is largely independent of the defect geometries, which validates the methodology of incorporating pre-defined defects in this study.

The fractured region was characterized from both top-down and cross-sectional perspectives. As shown in Fig. 5 (a), the top-down view reveals significant necking adjacent to the fracture site, which exhibits a highly zigzag morphology. Numerous cracks are distributed near the fracture zone. Given that these cracks were not present on the initial unpolished surface before testing, their emergences are attributed to the tensile deformation process. The high-magnification SEM images in Fig. 5 (b) and 5 (c) clearly show that voids exist beneath the crack on the specimen surface. Cross-sectional perspectives of the fracture surface are presented in Fig. 5 (d), revealing a high density of LPBF-induced defects. A more detailed view of typical fractured defects is provided in Fig. 5 (e). Pores featuring a distinct stair-case morphology and containing unmelted particles are observed, which has been reported in other researchers' works [4,12,42]. Additionally, deep cavities with highly rough internal surfaces can be found near these pores.

### 4.2. CA and ellipse-fitting method-based reconstructed microstructure

The model generated via the CA process is shown in Fig. 6 (a), within which the lamellar grain morphology elongated along the z-axis can be observed. A slice, which is highlighted by a red square and contains 11 grains, was extracted from the model for further study. It should be noted that the z-axis of the model is oriented vertically, which is perpendicular to the EBSD map of the actual material shown in Fig. 1 (c).

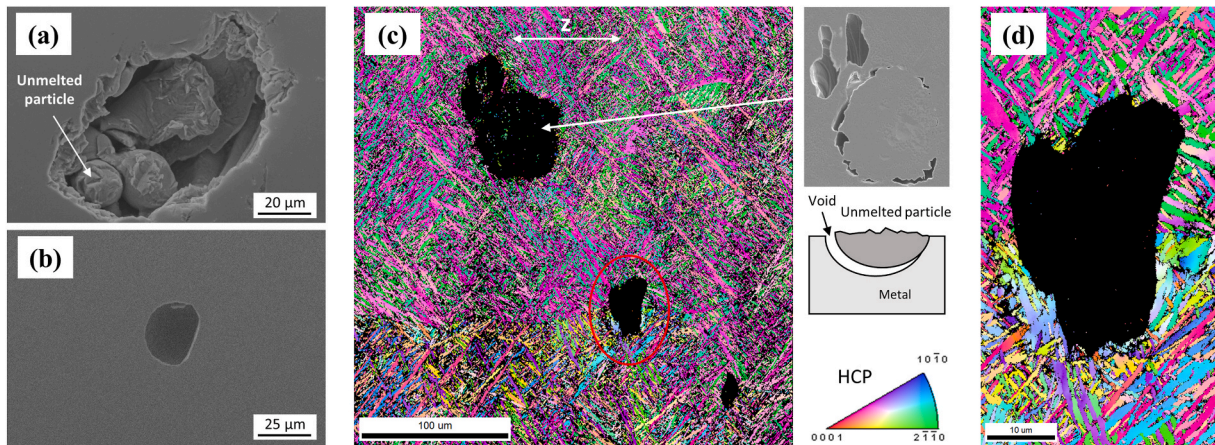


**Fig. 4.** SEM and EBSD characterization of LPBF-induced defects on the specimen surface. SEM images of (a) a lack-of-fusion defect and (b) gas-induced pore. (c) Low-magnification EBSD map acquired with a large step size, accompanied by a corresponding SEM image of the defect. (d) High-resolution EBSD map of the pore region obtained with a fine step size.

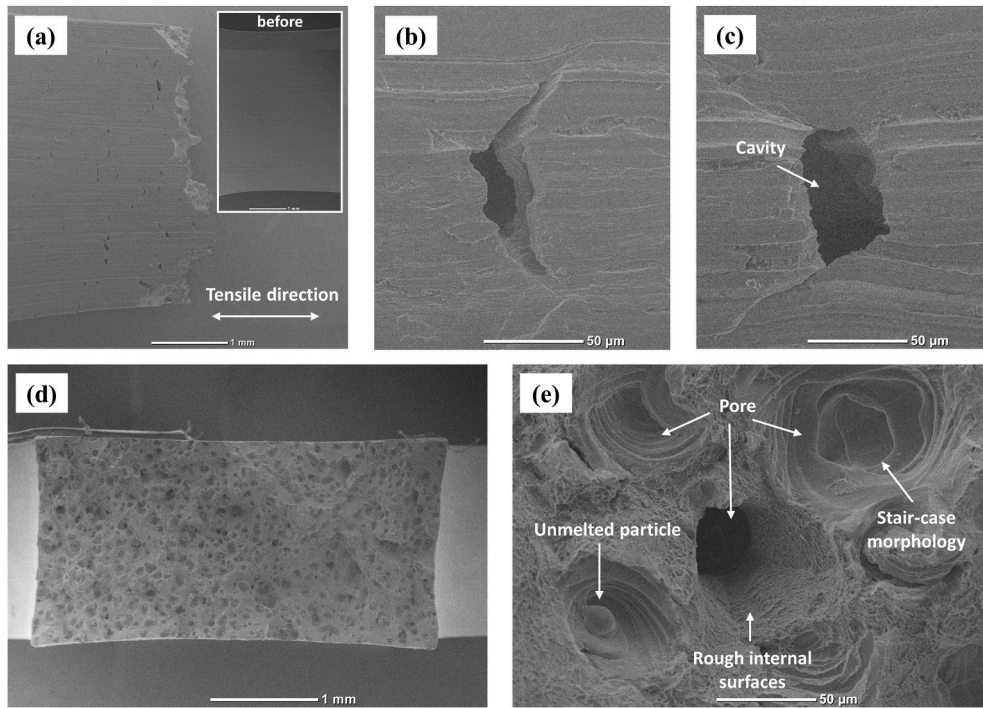
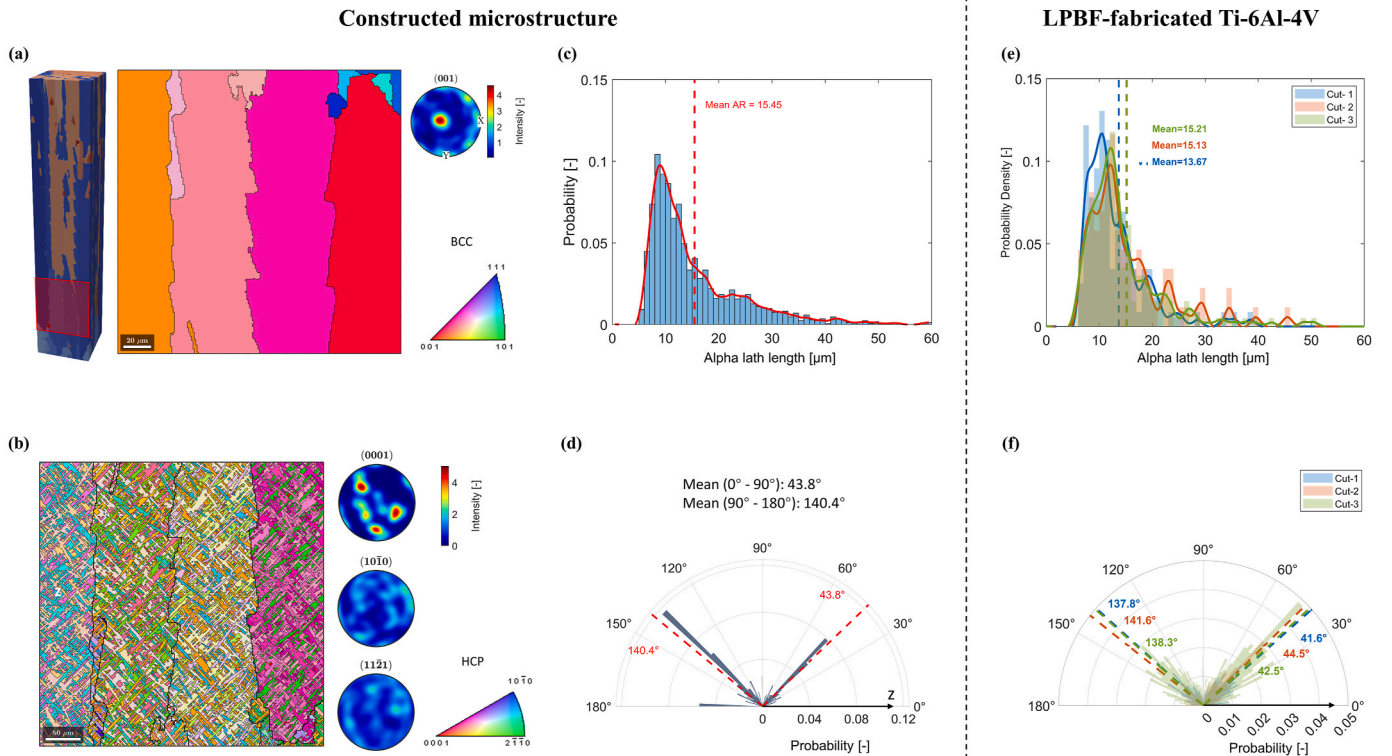


**Fig. 5.** SEM images of the fractured Ti-6Al-4V specimens. Top-down views: (a) overview of the fractured region attached with image before tensile test; (b, c) high-magnification images showing representative defects on the fracture surface. Cross-sectional views: (d) overview of the fractured region; (e) high-magnification images showing representative internal defects.





Although the actual material also exhibits a lamellar-like grain structure, its morphology has higher irregularity and topological complexity than the idealized grains produced by CA simulation. Nevertheless, the model successfully captures the essential lamellar features, providing a reliable approximation for subsequent crystal plasticity analysis. Furthermore, as shown in Fig. 6 (a), the CA model exhibits a texture intensity distribution in the PFs that is highly consistent with the reconstructed prior- $\beta$  grains in real LPBF-fabricated Ti-6Al-4V, further validating the crystallographic accuracy of the model.

The subsequent  $\alpha$ -lath substructure reconstruction within CA model was conducted based on the global morphological characteristics. The IPF and PFs of the model with the constructed  $\alpha$ -lath substructure are presented in Fig. 6 (b). Due to the constraints of the model size,  $\alpha$  phases with extremely fine grain sizes were excluded from the model to avoid any numerical artifacts. With the improved minimum elastic strain energy indicator rule, a more complex grain orientation was achieved, resulting in a texture intensity distribution that more closely aligns with the experimental data compared with our previous work [16], as shown in Fig. 1 (d). To quantitatively evaluate the model quality, the probability distributions of the  $\alpha$ -lath length and major-axis orientation relative to the z-axis are plotted in Fig. 6 (c) and 6 (d), respectively. The  $\alpha$ -lath length distribution shows excellent agreement with the actual material. However, the major-axis orientation distribution is more concentrated around two peak values compared to the experimental results. This discrepancy results from the fact that the number of  $\alpha$ -laths incorporated into the CA model is significantly lower than in the physical specimen. Furthermore, crossed  $\alpha$ -laths are treated as single grains in the current framework, which causes their morphology to be recognized as quasi-spherical and their orientations to gravitate toward  $180^\circ$ . Despite this, the mean lath orientations were calculated as  $43.8^\circ$  (within  $0^\circ$ – $90^\circ$ ) and  $140.4^\circ$  (within  $90^\circ$ – $180^\circ$ ), both of which are highly consistent with the observational results.

To ensure the statistical representativeness of the model, the spatial dependence of the  $\alpha$ -lath morphology from the crystal orientation of

individual prior- $\beta$  grains is verified. Three distinct regions were extracted from different prior- $\beta$  grains. Within these regions, the probability density of  $\alpha$ -lath length and inclination angle were calculated. As shown in Fig. 6 (e), the distribution of  $\alpha$ -lath length exhibits high consistency across the three sampled regions. Furthermore, these local distributions align closely with the overall distribution in terms of both statistical trends and mean values. A comparison between Figs. 6 (f) and Fig. 1 (f) confirms that the inclination angle between the major axis of the  $\alpha$ -laths and the BD remains relatively uniform at both local and global scales. These observations demonstrate that the morphological features of the  $\alpha$ -laths are not significantly biased by the orientation of the parent  $\beta$  grains. Consequently, the  $\alpha$ -lath substructure reconstruction matches both the global and local morphological characteristics of LPBF-fabricated Ti-6Al-4V.

#### 4.3. Crystal plasticity model with Monte Carlo method-based defect

A polygonal defect defined by 50 vertices was generated using the MC method, as illustrated in Fig. 7 (a). To validate the geometric fidelity of the model, nine key morphological parameters were calculated and compared against the experimentally measured averages, as shown in

**Table 2**  
Defect morphology evaluation.

Parameters	Measurement (Mean)	Defect model	Percentage deviation
Area [ $\mu\text{m}^2$ ]	1475.4	1349.2	8.5%
Perimeter [ $\mu\text{m}$ ]	159.8	158.8	0.6%
Major Axis [ $\mu\text{m}$ ]	49.5	47.1	5.8%
Minor Axis [ $\mu\text{m}$ ]	33.5	34.6	3.3%
Angle [ $^\circ$ ]	87.1	80.4	7.7%
Circularity [–]	0.66	0.7	6.1%
Aspect Ratio [–]	1.48	1.36	8.1%
Roundness [–]	0.67	0.734	6.4%
Solidity [–]	0.88	0.912	3.6%

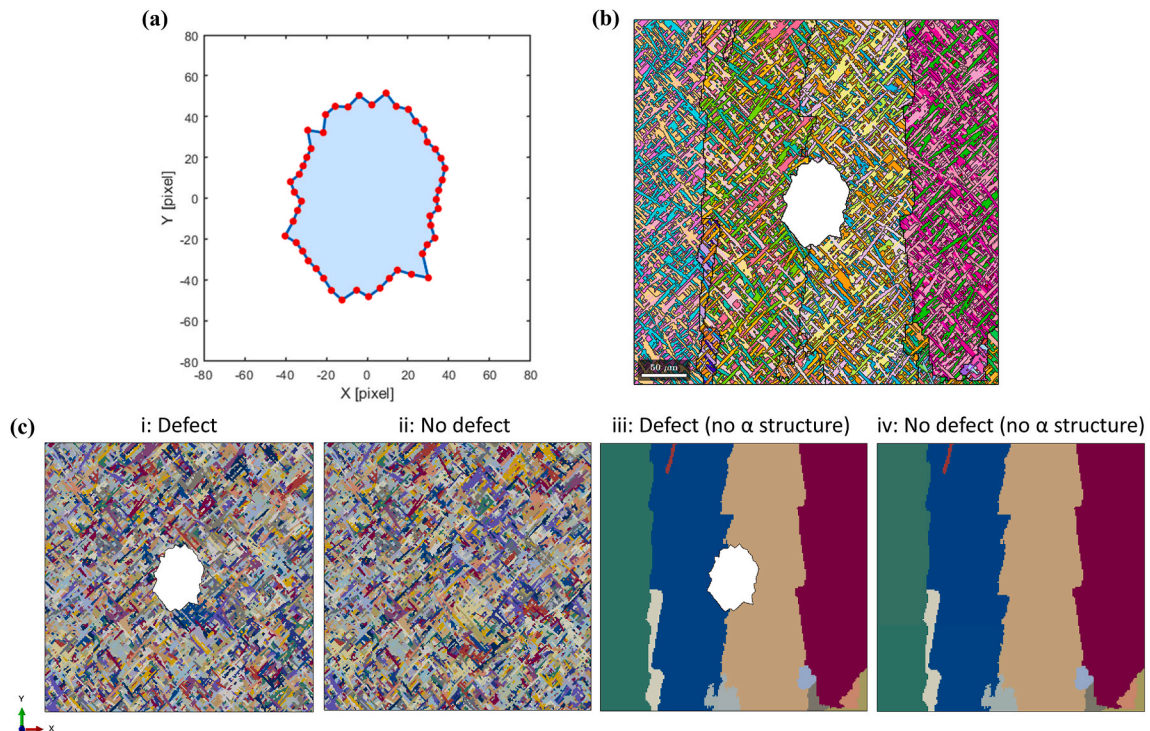


**Fig. 7.** Representative geometric and crystal plasticity models for CPFEM. (a) Morphology of a polygonal defect generated via the Monte Carlo method. (b) IPF of the  $\alpha$  phase substructure incorporated with a pre-designed defect. (c) Comparative input models in Abaqus: (i) model with defect and  $\alpha$ -lath substructure (DS), (ii) model without defect but with  $\alpha$ -lath substructure (NDS), (iii) model with defect but without  $\alpha$ -lath substructure (DNS), and (iv) model without defect and  $\alpha$ -lath substructure (NDNS).



**Table 2.** The generated defect shows high consistency with the experimental data across these parameters. Given that LPBF-induced defects exert no discernible influence on the  $\alpha$  microstructure, the generated defect is introduced to the center of the CA model. The four numerical models as discussed in Section 3.6 are shown in Fig. 7 (c).

To accurately capture the deformation behavior, the CP parameters were calibrated against the experimental stress-strain curves. Because the generated defect in the current study is relatively large compared to the overall model size, its inclusion during calibration would result in a significant underestimation of the intrinsic material strength. Therefore, the NDS model was selected for parameter calibration to ensure that the mechanical response of the material was accurately captured. Admittedly, since the experimental specimens inherently contain process-induced defects, the calibrated parameters may still deviate slightly from the absolute theoretical values. However, previous studies by H. Sun et al. [23] and J. Elambasseril et al. [13] have demonstrated that defects typically lead to only a marginal reduction in the yield strength and ultimate tensile strength. Furthermore, as the primary objective of this research is to investigate the localized mechanical responses of the defects and  $\alpha$ -lath substructures rather than the precise macroscopic predictions, this trade-off is considered acceptable for the current modeling framework.

The calibration results for the CP parameters are shown in Table 3. Among these parameters, the established and widely accepted constants, such as the elastic moduli  $C_{11}$ ,  $C_{12}$ ,  $C_{13}$ ,  $C_{33}$  and  $C_{44}$ , were referenced from the literature. In contrast, the CRSS parameters, which are sensitive to the dimensions and specific microstructure of the model, were calibrated within narrow bounds derived from previous studies [22,32,43]. The saturated CRSS and hardening parameters were iteratively adjusted to achieve an optimal fit with the experimental data, while maintaining values within a reasonable range. Reference slip rate and strain rate sensitivity were referenced from the literature.

#### 4.4. Tensile simulation

The tensile simulation results along with the experimental tensile test result are shown in Fig. 8. It can be observed that the NDS model achieves a good fit after the yield point, despite a slight deviation in the elastic region. Based on our previous research [16], the values for the elastic stiffness parameters have been proven reliable for simulating LPBF-fabricated Ti-6Al-4V. The observed deviation can be attributed to the high density of defects in the current specimens. These defects reduce the effective cross-sectional area relative to the nominal dimensions, leading to a lower elastic stiffness than the theoretical value.

**Table 3**  
CP parameters for Ti-6Al-4V alloys.

Parameters	$\alpha$ phase	Calibration
Elastic stiffness [GPa]	$C_{11}$	162.4
	$C_{12}$	92.0
	$C_{13}$	69.0
	$C_{33}$	180.7
	$C_{44}$	46.7
CRSS [MPa]	$\tau_0^{basal}$	370.0
	$\tau_0^{prismatic}$	326.0
	$\tau_0^{pyramidal<a>}$	431.8
	$\tau_0^{pyramidal<c+a>}$	520.0
	$\tau_0$	
Saturated CRSS [MPa]	$\tau_1$	$\tau_0 + 100.0$
Hardening parameters [MPa]	$b_1$	50.0
	$h_1$	500.0
Reference slip rate [–]	$\dot{\gamma}_0$	0.001
Strain rate sensitivity [–]	$\frac{1}{m}$	50

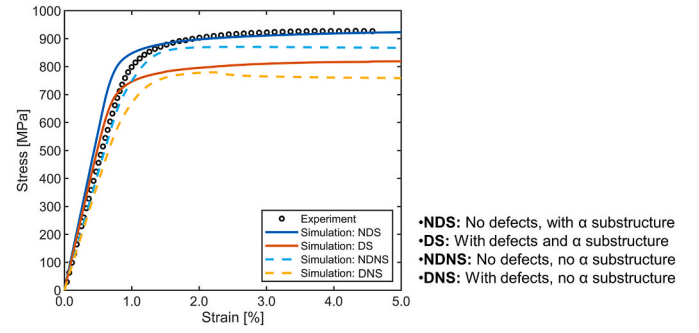


**Fig. 8.** Evaluation of four tensile simulation results against experimental data.

On the other hand, the fine  $\alpha$ -lath substructure can also lead to a significant increase in the elastic stiffness of the models. Although this discrepancy exists, it is considered acceptable as this study focuses primarily on the high-strain deformation regime.

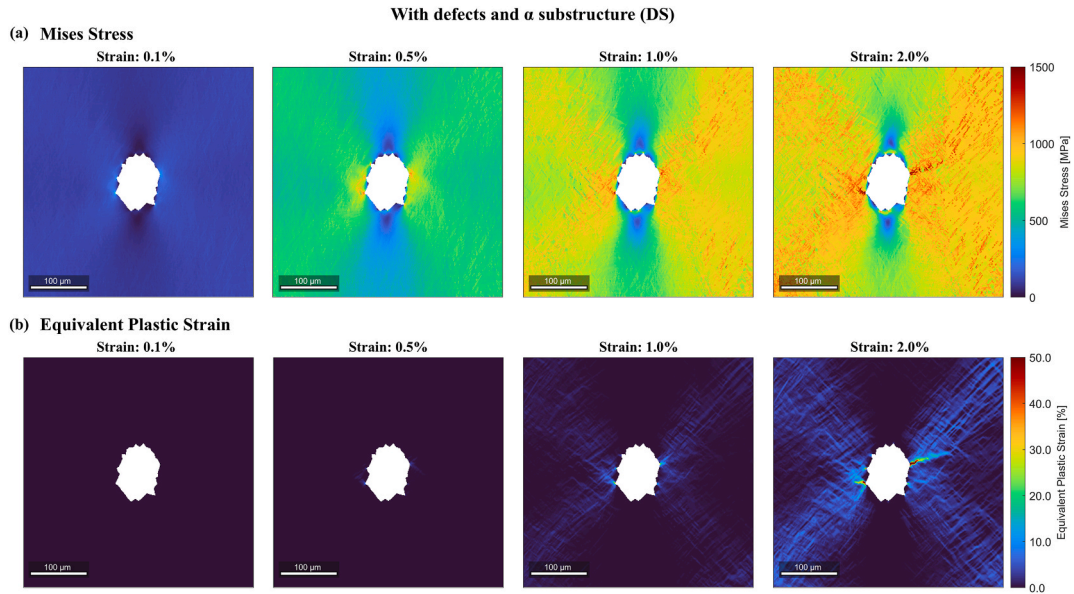
## 5. Discussion

### 5.1. Role of defect on tensile properties

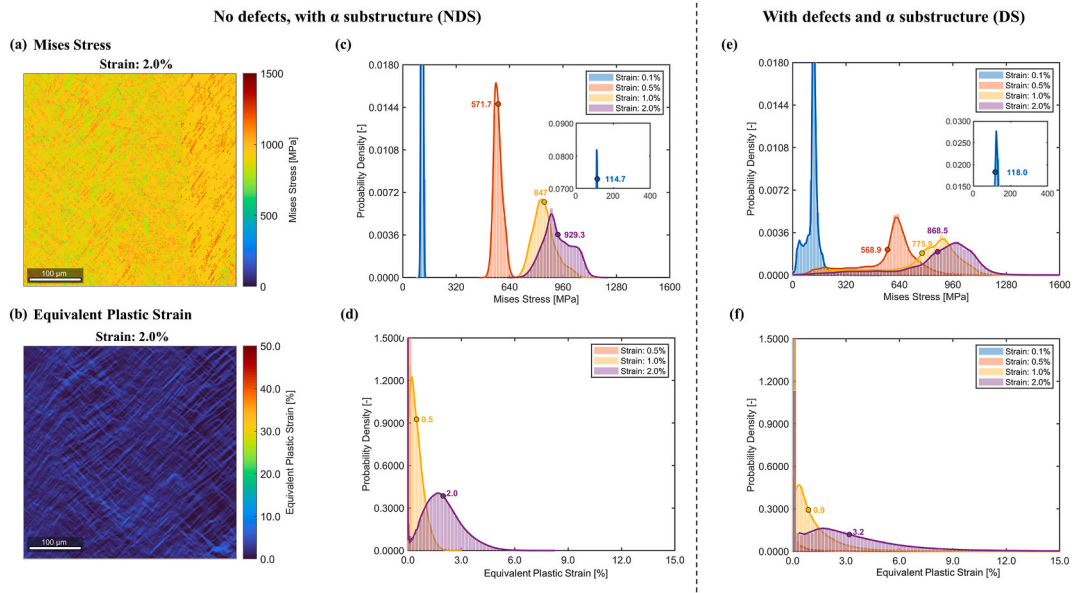
The von Mises stress maps at different global strain levels of the DS model levels are presented in Fig. 9 (a). The stress maps reveal low-stress zones located above and below the defect along the loading direction. Stress concentrations initiate as early as 0.1% global strain and intensify with increasing load. By 0.5% strain, stress concentration becomes evident near the sharp tips of the defect, even within the vertical low-stress regions. The most severe intensities are localized at the defect tips located transverse to the loading axis. When the global strain reaches 2.0%, these stress concentration zones elongate and propagate perpendicularly across adjacent  $\alpha$ -laths. As shown in Fig. 9 (b), the equivalent plastic strain localization only becomes prominent once the global strain reaches 1.0%. At this stage, the strain concentrates intensely along the 45° shear directions emanating from the defect center. A plastic strain band with higher than 50% of equivalent plastic strain can be observed, indicating the possibility of localized crack initiation at the defect tips as the material yields. As observed in Fig. 5, the fracture morphology of the hemispherical defects demonstrates that crack initiation and propagation preferentially occur from the median plane of the defect, aligning closely with the numerical simulation results. Furthermore, the asymmetry geometric distribution of the defect tips tends to induce two primary strain concentration regions, potentially leading to an inclined fracture path. This strain concentration likely serves as the origin of the zigzag morphology observed on the fractured surfaces.

In order to better understand the role of defects on tensile properties, the von Mises stress and equivalent plastic strain distribution maps at 2.0% global strain of NDS model levels are presented in Fig. 10 (a) and 10 (b), respectively. With no defect induced, both von Mises stress and equivalent plastic strain are relatively uniformly distributed in the model compared with the DS model. These results suggest that the  $\alpha$ -laths substructure alone does not induce any detrimental stress or strain concentrations.

To quantitatively evaluate the impact of defect while minimizing the effect of model boundary, a region of interest (ROI) of  $160 \times 160$  pixels was defined. The corresponding probability density distributions for the von Mises stress and equivalent plastic strain of the NDS model and the DS model are plotted in Fig. 10(c–f). As shown in Fig. 10 (c) and 10 (e), the presence of the defect leads to a noticeable broadening of the stress distribution and a reduction in the mean stress value. The expansion of the low-stress tail results from the existence of low-stress zones above and below the defect, while the high-stress tail is driven by intense concentrations at the defect tips. A similar trend is observed in the



**Fig. 9.** Evolution of von Mises stress and equivalent plastic strain distributions obtained from simulation result with DS model at global strain levels of 0.1%, 0.5%, 1.0% and 2.0%. (a) Von Mises stress distribution maps. (b) Equivalent plastic strain distribution maps.

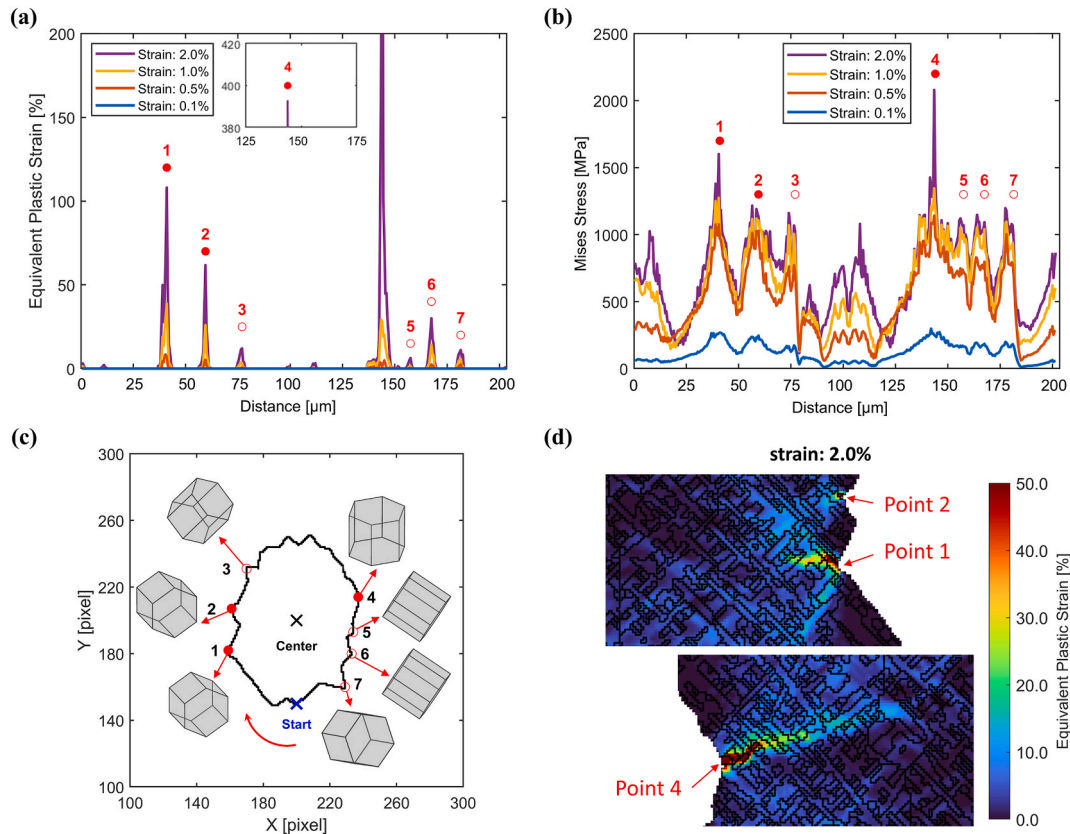


**Fig. 10.** Evaluation of simulation result with NDS model at global strain levels of 2.0%: (a) von Mises stress distribution maps and (b) equivalent plastic strain distribution maps. Probability density distributions within the ROI at global strain levels of 2.0% with mean values marked. NDS model: (c) von Mises stress and (d) equivalent plastic strain. DS model: (e) von Mises stress and (f) equivalent plastic strain.

equivalent plastic strain probability density as shown in Fig. 10 (d) and 10 (f), where the DS model exhibits a wider distribution spectrum compared to the NDS model. Notably, the mean equivalent plastic strain value for the DS model is significantly higher than that of the NDS model. This shift suggests that the presence of the defect not only induces large local stress differences but also accelerates the global plastic accumulation, leading to a more pronounced uneven deformation response.

The equivalent plastic strain and von Mises stress values along the defect boundary are plotted in Figs. 11 (a) and Fig. 11 (b) to study the effect of defect morphology on deformation response. The start position on the defect boundary and the direction of the path are illustrated in Fig. 11 (c). From the equivalent plastic strain distribution, seven distinct peaks, labeled as points 1 to 7, are observed. Among these points, three

peaks with higher values are defined as high strain points (HSPs), marked with solid red circles, while the remaining four are designated as low strain points (LSPs), marked with hollow red circles. Point 4 exhibits a significantly higher plastic strain than the other locations, identifying it as the most likely site for crack initiation. The positions of these peaks are also marked on the stress distribution plot. As expected, points 1 and 4 show high stress levels. However, point 2 exhibits a stress level nearly identical to the LSPs. Additionally, several points show high stress levels but almost no accumulated plastic strain. To better characterize these critical locations, the positions of the corresponding elements are displayed in Fig. 11 (c). The crystallographic orientations of specific  $\alpha$ -lath associated with these elements are also provided adjacent to each point. The equivalent plastic strain distribution map around the HSPs at 2.0% global strain is shown in Fig. 11 (d). The localized high-strain regions

With defects and  $\alpha$  substructure (DS)

**Fig. 11.** Quantitative analysis of the mechanical response along the defect boundary of DS model at global strain levels of 0.1%, 0.5%, 1.0%, and 2.0%. (a) Equivalent plastic strain and (b) von Mises stress profiles along the defect perimeter. (c) Schematic of the extraction path along the defect boundary, with the locations of the peak equivalent plastic strain highlighted. (d) Equivalent plastic strain distribution map around the HSPs at 2.0% global strain.

originate at the defect tips and subsequently propagate along the  $\alpha$ -lath over a short distance. Simultaneously, strain accumulation is observed to traverse across the  $\alpha$ -lath interfaces.

Wei S. et al. [45] successfully observed slip bands initiating from defect boundaries, suggesting that crack initiation likely originates from the localized accumulation of slip activity. In the crystal plasticity constitutive model, deformation is dominated by crystallographic slip behaviors, which are analyzed in detail below. To investigate the underlying mechanism on HSPs, the evolution of RSS/CRSS ratios for various slip systems relative to the global strain is presented in Fig. 12 (a), where cross marks denote the onset of slip activation (RSS/CRSS > 1). As discussed in Section 3.5, the CRSS increases during deformation due to strain-induced hardening. Thus, it is insufficient to determine the activation of a slip system solely by comparing the RSS and CRSS. Nevertheless, the RSS/CRSS ratio still serves as a critical indicator for interpreting the evolution of microscale slip activities. Points 1 and 2 exhibit similar variation trends across four slip systems. Notably, a decrease in the RSS/CRSS ratio is observed at point 1 around 0.7% global strain, likely attributable to lattice rotation and subsequent local stress redistribution. This phenomenon is more pronounced at point 4, where both prismatic and pyramidal  $\langle c+a \rangle$  slip systems show a distinct decline at 1.1% strain.

The accumulation of shear strains due to the activation of slip systems for each HSP are shown in Fig. 12 (b), with the start of shear strain accumulation is marked with circles. It is worth noting that incipient shear strain accumulation may occur even when RSS/CRSS < 1, as defined by the power-law flow rule in Eq. (8). Consistent with their RSS/CRSS profiles, points 1 and 2 show similar shear strain accumulation trends. Although the RSS/CRSS ratio of basal slip system at point 1

reaches the activation threshold at 0.7% strain, no significant shear strain is observed. To investigate the reason, the Schmid factors along the loading direction for various slip systems at the critical locations are shown in Table 4. It can be found that point 1 and 2 have a relatively low Schmid factor values at basal slip system, thereby suppressing strain accumulation despite the stress state. Similarly, while the prismatic system reaches a high RSS/CRSS ratio, it yields relatively low shear strain. This discrepancy can be attributed to its lower Schmid factor compared to the other two activated slip systems. In contrast, point 4 displays a distinct behavior. As illustrated in Fig. 11 (a) already, it exhibits highly localized plastic strain concentration, where basal slip dominates the initial stage before being surpassed by the rapid growth of the prismatic  $\langle a \rangle$  slip system.

For comparison, the RSS/CRSS ratios and accumulated shear strains for the four slip systems at LSPs are presented in Fig. 12 (c) and 12 (d), respectively. In contrast to the HSPs, point 3, 5 and 7 exhibit relatively low RSS/CRSS ratios and minimal shear strain accumulation, indicating that the slip systems at these locations are seldom activated. Among these points, prismatic and pyramidal  $\langle c+a \rangle$  slip systems are the primary contributors to the slip behaviors. Only point 6 displays an RSS value exceeding the CRSS threshold, which correlates with a higher observed shear strain. As illustrated in Fig. 11 (a), point 6 exhibits a significantly higher equivalent plastic strain value than other three LSPs, which approaches the levels of HSPs. A high level of basal slip and pyramidal  $\langle a \rangle$  slip activities can be observed.

By analyzing these slip behaviors, it is evident that the dominant slip systems vary significantly along the defect boundaries. Although stress concentration is a common feature at defect tips, the actual magnitude of strain accumulation is primarily governed by the specific types of



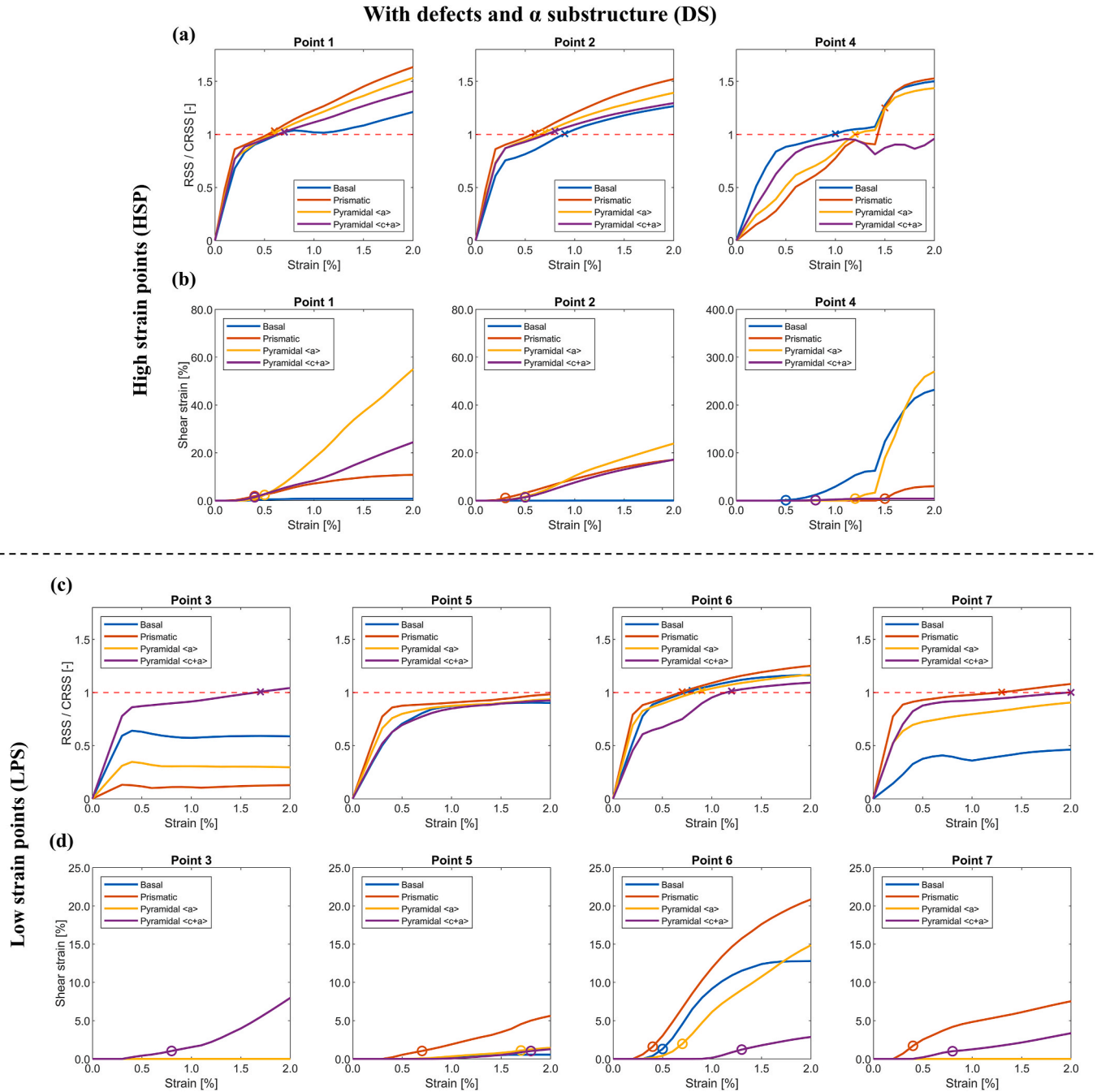


**Fig. 12.** Local micromechanical evolution at the HSPs locations along the defect boundary of DS model. (a) RSS/CRSS ratios and (b) accumulated shear strain of different slip along with global strain. Local micromechanical evolution at the LSPs locations along the defect boundary of DS model. (c) RSS/CRSS ratios and (d) accumulated shear strain of different slip along with global strain.

**Table 4**

Schmid factors along with loading direction for various slip systems at the critical locations.

Slip systems	Large strain points			Small strain points			
	Point 1	Point 2	Point 4	Point 3	Point 5	Point 6	Point 7
Basal	0.345	0.345	0.421	0.444	0.448	0.448	0.084
Prismatic	0.420	0.420	0.121	0.342	0.343	0.343	0.475
Pyramidal <a>	0.475	0.475	0.242	0.463	0.459	0.459	0.452
Pyramidal <c + a>	0.467	0.467	0.483	0.394	0.391	0.391	0.466

activated slip systems. Specifically, tips characterized by low strain levels tend to be dominated by prismatic and pyramidal  $\langle c+a \rangle$  slip systems. Conversely, tips exhibiting high strain localization are typically dominated by basal and pyramidal  $\langle a \rangle$  slip systems, which will likely become the origins of crack initiation.

## 5.2. Interaction between two defects

To examine the cross-sectional morphology of the defects located at the fracture edges, the fractured specimens were repolished, with a layer of several tens of micrometers carefully removed. The optical microscopic images of the fracture edges containing multiple process-induced defects are shown in Fig. 13 (a). Two distinct spatial arrangements of



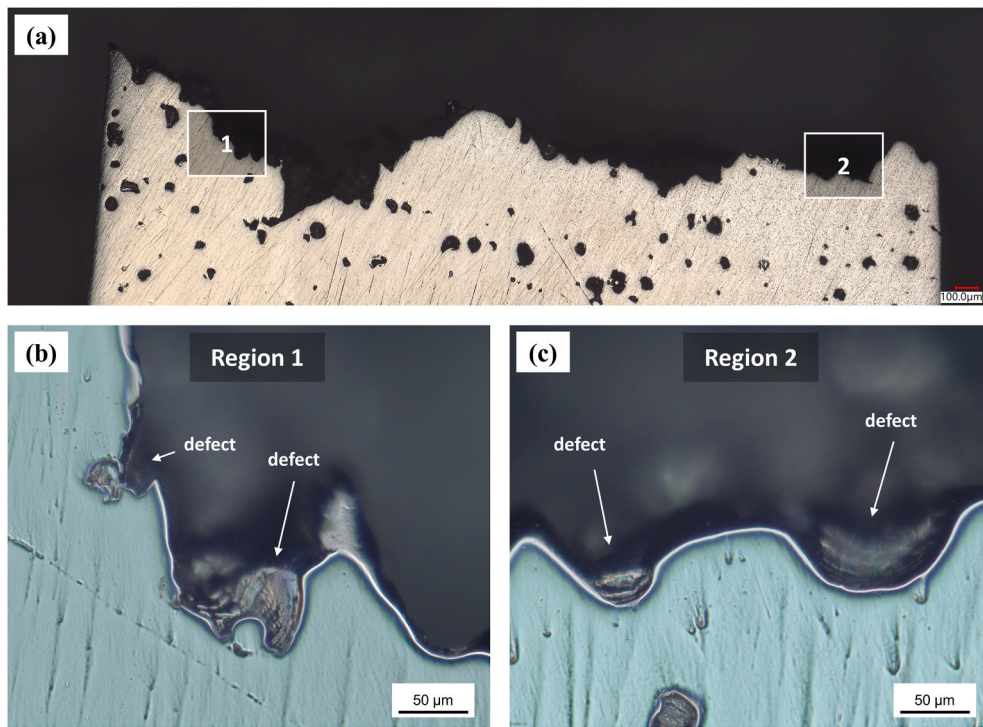


**Fig. 13.** Optical microscopic images of the fracture edges containing multiple process-induced defects. (a) overall view of fractured surface, (b) diagonal spatial distribution and (c) transverse spatial distribution.

adjacent defects are observed: diagonal distribution and transverse distribution, as shown in Fig. 13 (b) and 13 (c), respectively. It is evident that the fracture typically initiates at a primary defect and subsequently propagates toward adjacent defects. This process of crack linkage between neighboring voids results in a characteristic zigzag morphology of the fractured surface.

To investigate the synergistic effects of multiple defects on the tensile response, three DS-based models, in which a secondary defect is placed at transverse (right), diagonal (upper-right), and longitudinal (upper) positions of the central defect relative to the loading direction, are used to conduct CPFEM simulations under identical conditions. These secondary defects, generated via the MC method, were characterized by smaller surface areas. The resulting von Mises stress and equivalent plastic strain distribution maps at 2.0% global strain are shown in Fig. 14 (a) and 14 (b), respectively. Observations reveal that when the secondary defect is positioned perpendicular to the loading direction, an intense stress and strain band connecting two defects is formed. This configuration significantly alters the global field, as strain accumulation becomes highly constrained within the ligament between the defects, as well as the region between secondary defect and the model boundary. However, as the secondary defect shifts to a position aligned with the loading direction, this interactive band weakens and eventually disappears. Notably, the presence of a secondary defect appears to have a negligible impact on the stress and strain distribution on the opposite side of the primary defect.

The equivalent plastic strain and von Mises stress values along the defect boundary are plotted in Fig. 14 (c) and 14 (d), respectively. It is evident that the introduction of secondary defects markedly influences the local stress and strain distribution, particularly at point 4, which is identified as a primary site for crack initiation. Specifically, when the secondary defect is in a transverse position, a relative decrease in stress is observed at point 4. However, as the secondary defect shifts toward a longitudinal alignment with the loading direction, the stress levels at point 4 consistently rise, leading to a more pronounced accumulation of equivalent plastic strain. This suggests that secondary defects can significantly accelerate the crack initiation process by causing severer

stress localization. Notably, in the transverse configuration, although the equivalent plastic strain at point 4 is comparable to that observed in the single-defect DS model, a significantly higher strain concentration occurs within the boundary of the secondary defect.

### 5.3. Effects of $\alpha$ phase substructure

To investigate the influence of  $\alpha$ -lath substructure, the von Mises stress and equivalent plastic strain distribution maps of DNS model are shown in Fig. 15 (a) and 15 (b), respectively. Although similarities can be found in the stress and strain concentration at the tips of defects like NDS model, significant localization is also identified along the prior- $\beta$  grain boundaries. In the absence of  $\alpha$ -lath substructure, both stress and strain distributions appear more homogeneous and exhibit a high sensitivity to prior- $\beta$  grain colonies. Notably, the characteristic lath-shaped strain bands extending from the defect tips, which are prominent in the DS model, are absent here. However, even without the inclusion of  $\alpha$ -lath substructure, the presence of defects inherently leads to a heterogeneous stress and strain field in the ROI, as shown in Fig. 15 (c) and 15 (d). It is noteworthy that the stress distribution tends to exhibit bimodal peaks with a lower mean value, whereas the overall strain distribution concentrates within a low-magnitude regime.

The equivalent plastic strain and von Mises stress values along the defect boundary of DNS model are plotted in Fig. 15(e) and 15 (f), respectively. While strain concentrations are observed at the defect tips, their peak magnitudes are significantly lower and more uniform compared to those in the DS model. Specifically, in the presence of  $\alpha$ -lath substructure, the critical point 4 exhibits an extremely high strain concentration, identifying it as the most probable site for crack initiation. Conversely, in the absence of the  $\alpha$ -lath substructure, the maximum strain concentration shifts to point 1, accompanied by a substantial reduction in magnitude. Similarly, stress concentrations at corresponding locations undergo a marked decrease. Consequently, the prediction based on models with  $\alpha$ -lath substructure neglected can lead to severe deviations from the actual mechanical response.

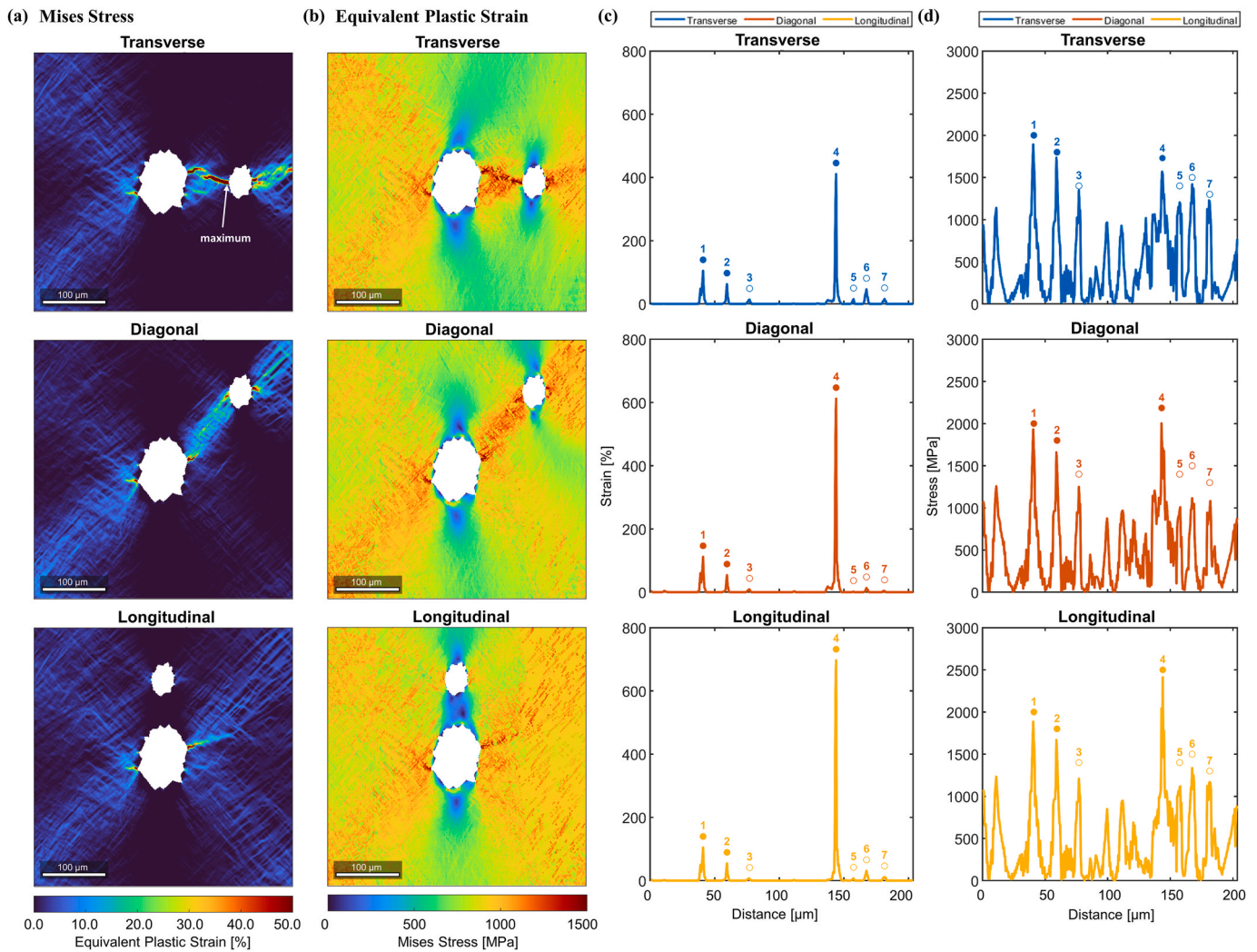


**Fig. 14.** The tensile responses of DS model with a secondary defect at transverse, diagonal and longitudinal sides of the central defect at 2.0% global strain. (a) Von Mises stress distribution maps. (b) Equivalent plastic strain distribution maps. (c) Equivalent plastic strain and (d) von Mises stress profiles along the defect perimeter.

#### 5.4. Future approaches

In this study, a quasi-2D model with a thickness of  $0.5\ \mu\text{m}$  was employed for the CPFEM simulations. As the primary objective of this research is to improve the traditional digital modeling methods and propose a novel approach based on the morphological characteristics of LPBF-fabricated Ti-6Al-4V microstructures, the use of a 2D model is considered acceptable for demonstrating the effectiveness of the algorithm. While 2D modeling remains a prevalent and effective method for identifying fundamental slip system activation and strain localization trends, it must be acknowledged that a 2D simplification inherently neglects the out-of-plane dislocation movements and the complex 3D connectivity of the pore network, which may lead to a slight overestimation of local stress magnitudes [13]. Additionally, strain rate and temperature are widely known factors influencing the mechanical response for LPBF-fabricated Ti-6Al-4V [32,46]. Therefore, extending the current framework into a fully 3D multiscale model that incorporates these thermal and rate-dependent factors represents a critical direction for future research.

#### 6. Conclusions

A novel approach integrating cellular automata with an algorithm-based structure generation is proposed to address the underestimation

of microstructural homogeneity that is often encountered in numerical investigations of LPBF-fabricated Ti-6Al-4V alloy. Through a comparative study between experimental and simulation results, associated with slip behavior analysis, the synergistic roles of the  $\alpha$ -lath substructure and process-induced defects on the resulting tensile responses are systematically evaluated. The primary conclusions of this study can be summarized as follows:

- (1) The proposed CA-based and algorithm-driven modeling methodology effectively reproduces the morphological characteristics of LPBF-fabricated Ti-6Al-4V microstructures.
- (2) The Monte Carlo-based approach is demonstrated to be a feasible tool for generating polygonal defects that exhibit high consistency with experimental data across nine distinct morphological parameters.
- (3) The presence of defects not only enhances local stress differences but also accelerates the global plastic accumulation. These high-strain regions originate at defect tips and subsequently propagate along  $\alpha$ -laths, traversing phase interfaces over short distances.
- (4) Defect tips with lower strain levels are primarily influenced by prismatic and pyramidal  $\langle c+a \rangle$  slip systems. Conversely, tips exhibiting high strain localization are typically governed by basal and pyramidal  $\langle a \rangle$  slip systems, identifying these locations as the most probable sites for crack initiation.



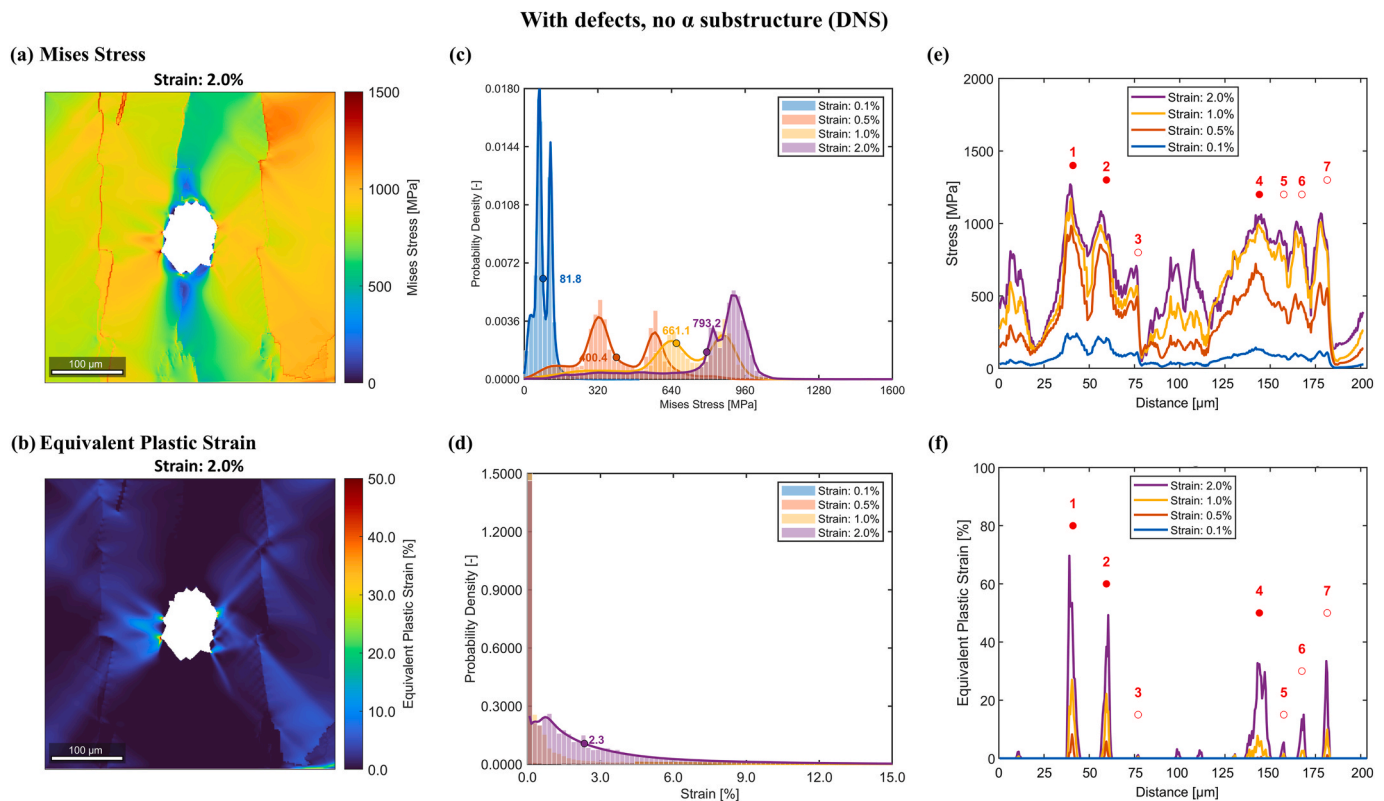


**Fig. 15.** Evaluation of simulation result with DNS model: (a) von Mises stress distribution maps and (b) equivalent plastic strain distribution maps at global strain levels of 2.0%. Probability density distributions within the ROI at different global strain levels: (c) von Mises stress; (d) Equivalent plastic strain. Mechanical response along the defect boundary of DNS model at global strain levels of 0.1%, 0.5%, 1.0%, and 2.0%: (e) equivalent plastic strain and (f) von Mises stress profiles along the defect perimeter. (Highlighted points correspond to the same critical locations in the DS model.)

(5) Multi-defect interaction simulations demonstrate that secondary defects are harmful to structural integrity and facilitate strain localization between defects, thereby significantly accelerating the onset of localized failure and resulting in a zigzag-shaped fracture surface.

(6) The incorporation of the  $\alpha$ -lath substructure significantly enhances both the predicted model stiffness and the ultimate tensile strength. Neglecting the  $\alpha$ -lath substructure results in a stress distribution overly dependent on prior- $\beta$  grain boundaries and a marked underestimation of local stress and strain concentrations. Such simplifications lead to significant deviations in predicting the tensile properties and failure mechanisms of LPBF-fabricated Ti-6Al-4V alloy.

#### CRediT authorship contribution statement

**Hanqing Liu:** Conceptualization, Data curation, Formal analysis, Investigation, Methodology, Software, Validation, Visualization, Writing – original draft. **Fabien Briffod:** Software, Writing – review & editing. **Takayuki Shiraiwa:** Funding acquisition, Project administration, Supervision, Writing – review & editing.

#### Declaration of competing interest

The authors declare that they have no known competing financial interests or personal relationships that could have appeared to influence the work reported in this paper.

#### Acknowledgments

The authors acknowledge the financial support by JST SPRING,

Grant Number JPMJSP2108, JSPS KAKENHI Grant-in-Aid for Transformative Research Areas (A) (Grant No. 24H00982), the Amada Foundation (Grant No. AF-2025212-B2), the NSK Foundation for the Advancement of Mechatronics, and the Japan Welding Engineering Society (JWES).

#### Data availability

The raw/processed data are available from the corresponding author upon reasonable request.

#### References

- [1] J. Plocher, A. Panesar, Review on design and structural optimisation in additive manufacturing: towards next-generation lightweight structures, *Mater. Des.* 183 (2019) 108164, <https://doi.org/10.1016/j.matdes.2019.108164>.
- [2] M. Abdel-Hady Gepreel, M. Niinomi, Biocompatibility of Ti-alloys for long-term implantation, *J. Mech. Behav. Biomed. Mater.* 20 (2013) 407–415, <https://doi.org/10.1016/j.jmbbm.2012.11.014>.
- [3] L. Bai, C. Gong, X. Chen, Y. Sun, J. Zhang, L. Cai, et al., Additive manufacturing of customized metallic orthopedic implants: materials, structures, and surface modifications, *Metals* 9 (2019) 1004, <https://doi.org/10.3390/met9091004>.
- [4] Z. Li, C. Affolter, High-cycle fatigue performance of laser powder bed fusion Ti-6Al-4V alloy with inherent internal defects: a critical literature review, *Metals* 14 (2024) 972, <https://doi.org/10.3390/met14090972>.
- [5] D. Agius, K.I. Kourousis, C. Wallbrink, A review of the As-Built SLM Ti-6Al-4V mechanical properties towards achieving fatigue resistant designs, *Metals* 8 (2018) 75, <https://doi.org/10.3390/met8010075>.
- [6] J.-B. Lee, D. Seo, H.Y. Chang, Evaluating corrosion resistance of additive-manufactured Ti-6Al-4V using electrochemical critical localized corrosion temperature, *Met. Mater. Int.* 26 (2020) 39–45, <https://doi.org/10.1007/s12540-019-00484-z>.
- [7] S. Liu, Y.C. Shin, Additive manufacturing of Ti6Al4V alloy: a review, *Mater. Des.* 164 (2019) 107552, <https://doi.org/10.1016/j.matdes.2018.107552>.
- [8] C. Ni, J. Zhu, B. Zhang, K. An, Y. Wang, D. Liu, et al., Recent advance in laser powder bed fusion of Ti-6Al-4V alloys: microstructure, mechanical properties and

- machinability, *Virtual Phys. Prototyp.* 20 (2025) e2446952, <https://doi.org/10.1080/17452759.2024.2446952>.
- [9] Z. Xu, A. Liu, X. Wang, Fatigue performance differences between rolled and selective laser melted Ti6Al4V alloys, *Mater. Charact.* 189 (2022) 111963, <https://doi.org/10.1016/j.matchar.2022.111963>.
  - [10] J. Yang, H. Yu, J. Yin, M. Gao, Z. Wang, X. Zeng, Formation and control of martensite in Ti-6Al-4V alloy produced by selective laser melting, *Mater. Des.* 108 (2016) 308–318, <https://doi.org/10.1016/j.matdes.2016.06.117>.
  - [11] T. Voisin, N.P. Calta, S.A. Khairallah, J.-B. Forien, L. Balogh, R.W. Cunningham, et al., Defects-dictated tensile properties of selective laser melted Ti-6Al-4V, *Mater. Des.* 158 (2018) 113–126, <https://doi.org/10.1016/j.matdes.2018.08.004>.
  - [12] A. Gupta, C.J. Bennett, W. Sun, The role of defects and characterisation of tensile behaviour of EBM additive manufactured Ti-6Al-4V: an experimental study at elevated temperature, *Eng. Fail. Anal.* 120 (2021) 105115, <https://doi.org/10.1016/j.engfailanal.2020.105115>.
  - [13] J. Elambasseril, S.L. Lu, Y.P. Ning, N. Liu, J. Wang, M. Brandt, et al., 3D characterization of defects in deep-powder-bed manufactured Ti-6Al-4V and their influence on tensile properties, *Mater. Sci. Eng., A* 761 (2019) 138031, <https://doi.org/10.1016/j.msea.2019.138031>.
  - [14] L. Bhandari, V. Gaur, On study of process induced defects-based fatigue performance of additively manufactured Ti6Al4V alloy, *Addit. Manuf.* 60 (2022) 103227, <https://doi.org/10.1016/j.addma.2022.103227>.
  - [15] J. Liu, K. Zhang, J. Liu, R. Zhang, Z. Zeng, Y. Zhu, et al., Discovering the role of the defect morphology and microstructure on the deformation behavior of additive manufactured Ti-6Al-4V, *Mater. Sci. Eng., A* 859 (2022) 144202, <https://doi.org/10.1016/j.msea.2022.144202>.
  - [16] H. Liu, M. Kitamura, F. Briffod, T. Shiraiwa, A cellular automata-based crystal plasticity analysis of slip activity in additive manufactured Ti-6Al-4V during dwell fatigue, *J. Alloys Compd.* 1041 (2025) 183867, <https://doi.org/10.1016/j.jallcom.2025.183867>.
  - [17] S.L. Semiatin, V. Seetharaman, I. Weiss, The thermomechanical processing of alpha/beta titanium alloys, *JOM* 49 (1997) 33–39, <https://doi.org/10.1007/BF02914711>.
  - [18] Y. Chong, G. Deng, S. Gao, J. Yi, A. Shibata, N. Tsuji, Yielding nature and hall-petch relationships in Ti-6Al-4V alloy with fully equiaxed and bimodal microstructures, *Scr. Mater.* 172 (2019) 77–82, <https://doi.org/10.1016/j.scriptamat.2019.07.015>.
  - [19] P.-H. Li, W.-G. Guo, W.-D. Huang, Y. Su, X. Lin, K.-B. Yuan, Thermomechanical response of 3D laser-deposited Ti-6Al-4V alloy over a wide range of strain rates and temperatures, *Mater. Sci. Eng., A* 647 (2015) 34–42, <https://doi.org/10.1016/j.msea.2015.08.043>.
  - [20] A. Azarniya, X.G. Colera, M.J. Mirzaali, S. Sovizi, F. Bartolomeu, M. St Węglowski, et al., Additive manufacturing of Ti-6Al-4V parts through laser metal deposition (LMD): process, microstructure, and mechanical properties, *J. Alloys Compd.* 804 (2019) 163–191, <https://doi.org/10.1016/j.jallcom.2019.04.255>.
  - [21] G. Lütjering, Property optimization through microstructural control in titanium and aluminum alloys, *Mater. Sci. Eng., A* 263 (1999) 117–126, [https://doi.org/10.1016/S0921-5093\(98\)01169-1](https://doi.org/10.1016/S0921-5093(98)01169-1).
  - [22] F. Bridier, D.L. McDowell, P. Villechaise, J. Mendez, Crystal plasticity modeling of slip activity in Ti-6Al-4V under high cycle fatigue loading, *Int. J. Plast.* 25 (2009) 1066–1082, <https://doi.org/10.1016/j.ijplas.2008.08.004>.
  - [23] H. Sun, E.P. Busso, C. Ling, D.-F. Li, Crystal plasticity based investigation of the effects of additive manufactured voids on the strain localisation behaviour of Ti-6Al-4V, *Int. J. Plast.* 183 (2024) 104141, <https://doi.org/10.1016/j.ijplas.2024.104141>.
  - [24] X. Chen, J. Zhang, L. Hu, D. Ji, Investigation on anisotropic behavior of additively manufactured Ti-6Al-4V based on cellular automaton and CPFEM, *Met. Mater. Int.* (2025), <https://doi.org/10.1007/s12540-025-01902-1>.
  - [25] F. Briffod, T. Shiraiwa, M. Enoki, Microstructure modeling and crystal plasticity simulations for the evaluation of fatigue crack initiation in  $\alpha$ -iron specimen including an elliptic defect, *Mater. Sci. Eng., A* 695 (2017) 165–177, <https://doi.org/10.1016/j.msea.2017.04.030>.
  - [26] M. Rolchigo, S.T. Reeve, B. Stump, G.L. Knapp, J. Coleman, A. Plotkowski, et al., ExaCA: a performance portable exascale cellular automata application for alloy solidification modeling, *Comput. Mater. Sci.* 214 (2022) 111692, <https://doi.org/10.1016/j.commatsci.2022.111692>.
  - [27] L. Lach, Cellular automata and phase-field modeling of microstructure evolution in metal additive manufacturing: recent advances, hybrid frameworks, and pathways to predictive control, *Metals* 16 (2026) 124, <https://doi.org/10.3390/met16010124>.
  - [28] H. Gu, Y. Fu, C. Wei, L. Li, L. Qian, W. Zhou, et al., The impact of thermocapillary on equiaxed/columnar microstructure evolution in laser powder bed fusion: a high-fidelity ray-tracing based finite volume and cellular automaton study, *J. Mater. Process. Technol.* 326 (2024) 118335, <https://doi.org/10.1016/j.jmatprotec.2024.118335>.
  - [29] D. De Baere, S. Mohanty, J.H. Hattel, Microstructural modelling of above  $\beta$ -transus heat treatment of additively manufactured Ti-6Al-4V using cellular automata, *Mater. Today Commun.* 24 (2020) 101031, <https://doi.org/10.1016/j.mtcomm.2020.101031>.
  - [30] X. Cai, K. Tang, P. Ferro, F. Berto, Coordinated effect of microstructure and defect on fatigue accumulation in dual-phase Ti-6Al-4V: quantitative characterization, *Int. J. Fatig.* 167 (2023) 107305, <https://doi.org/10.1016/j.ijfatigue.2022.107305>.
  - [31] K. Tiwari, A. Trivedi, B. Reddy, B.K. Kumawat, A. Bhardwaj, R.K.S. Raman, et al., Crystal plasticity modeling and data-driven approach for fatigue life estimation of additively manufactured Ti-6Al-4V alloy, <https://doi.org/10.2139/ssrn.4946708>, 2024.
  - [32] L. Yin, O. Umezawa, Crystal plasticity analysis of temperature-sensitive dwell fatigue in Ti-6Al-4V titanium alloy for an aero-engine fan disc, *Int. J. Fatig.* 156 (2022) 106688, <https://doi.org/10.1016/j.ijfatigue.2021.106688>.
  - [33] W.G. Burgers, On the process of transition of the cubic-body-centered modification into the hexagonal-close-packed modification of zirconium, *Physica* 1 (1934) 561–586, [https://doi.org/10.1016/S0031-8914\(34\)80244-3](https://doi.org/10.1016/S0031-8914(34)80244-3).
  - [34] F. Briffod, T. Shiraiwa, M. Enoki, S. Emura, Effect of macrozones on fatigue crack initiation and propagation mechanisms in a forged ti-6Al-4V alloy under fully-reversed condition, *Materialia* 22 (2022) 101401, <https://doi.org/10.1016/j.mtla.2022.101401>.
  - [35] C. Lavogiez, S. Hémery, P. Villechaise, Analysis of deformation mechanisms operating under fatigue and dwell-fatigue loadings in an  $\alpha/\beta$  titanium alloy, *Int. J. Fatig.* 131 (2020) 105341, <https://doi.org/10.1016/j.ijfatigue.2019.105341>.
  - [36] E.O. Hall, The deformation and ageing of mild steel: III discussion of results, *Proc. Phys. Soc. B* 64 (1951) 747–753, <https://doi.org/10.1088/0370-1301/64/9/303>.
  - [37] T.L. Richards, The geometry of the plastic deformation of polycrystalline aggregates, *Rheol. Acta* 2 (1962) 1–9, <https://doi.org/10.1007/BF01972547>.
  - [38] J.R. Mayeur, D.L. McDowell, A three-dimensional crystal plasticity model for duplex Ti-6Al-4V, *Int. J. Plast.* 23 (2007) 1457–1485, <https://doi.org/10.1016/j.ijplas.2006.11.006>.
  - [39] F. Briffod, T. Shiraiwa, M. Enoki, Nucleation and propagation modeling of short fatigue crack in rolled bi-modal Ti-6Al-4V alloy, *Mater. Sci. Eng., A* 790 (2020) 139710, <https://doi.org/10.1016/j.msea.2020.139710>.
  - [40] S. Tammis-Williams, H. Zhao, F. Léonard, F. Derguti, I. Todd, P.B. Prangnell, XCT analysis of the influence of melt strategies on defect population in Ti-6Al-4V components manufactured by selective electron beam melting, *Mater. Charact.* 102 (2015) 47–61, <https://doi.org/10.1016/j.matchar.2015.02.008>.
  - [41] S.A. Khairallah, A.T. Anderson, A. Rubenchik, W.E. King, Laser powder-bed fusion additive manufacturing: physics of complex melt flow and formation mechanisms of pores, spatter, and denudation zones, *Acta Mater.* 108 (2016) 36–45, <https://doi.org/10.1016/j.actamat.2016.02.014>.
  - [42] M. Bonneric, N. Saintier, D. El Khoukhi, J. Bega, Influence of the defect size, type, and position on the high cycle fatigue behavior of Ti-6Al-4V processed by laser powder bed fusion, *Int. J. Fatig.* 193 (2025) 108783, <https://doi.org/10.1016/j.ijfatigue.2024.108783>.
  - [43] K. Kapoor, P. Ravi, R. Noraas, J.-S. Park, V. Venkatesh, M.D. Sangid, Modeling Ti-6Al-4V using crystal plasticity, calibrated with multi-scale experiments, to understand the effect of the orientation and morphology of the  $\alpha$  and  $\beta$  phases on time dependent cyclic loading, *J. Mech. Phys. Solid.* 146 (2021) 104192, <https://doi.org/10.1016/j.jmps.2020.104192>.
  - [44] Y. Zhao, K. Tang, P. Ferro, F. Berto, Crystal plasticity modeling fatigue behavior in bimodal Ti-6Al-4V: effects of microdefect and lamellar orientation, *Fatig. Fract. Eng. Mater. Struct.* 47 (2024) 2195–2214, <https://doi.org/10.1111/ffe.14292>.
  - [45] W. Sun, M. Li, H. Li, On defect evolution in EBM additively manufactured Ti-6Al-4V via in situ investigations, *Materials* 17 (2024) 2888, <https://doi.org/10.3390/ma17122888>.
  - [46] Z. Zheng, P. Zhao, M. Zhan, S. Shen, Y. Wang, M.W. Fu, The roles of rise and fall time in load shedding and strain partitioning under the dwell fatigue of titanium alloys with different microstructures, *Int. J. Plast.* 149 (2022) 103161, <https://doi.org/10.1016/j.ijplas.2021.103161>.